

22. LATE MIocene–HOLOCENE MAGNETIC POLARITY STRATIGRAPHY AND ASTROCHRONOLOGY, ODP LEG 198, SHATSKY RISE¹

Helen F. Evans,² James E.T. Channell,² and William W. Sager³

ABSTRACT

Shatsky Rise, a medium-sized large igneous province in the west Central Pacific Ocean, has three main topographic highs that preserve a thick sedimentary record from Cretaceous through Cenozoic. During Ocean Drilling Program (ODP) Leg 198 to Shatsky Rise, a total of ~768 m of late Miocene–Holocene sediments was recovered from six sites. Sites 1207 and 1208 were drilled on the Northern and Central Highs, respectively, and yielded expanded late Miocene–Holocene sequences. Sites 1209, 1210, 1211, and 1212 were drilled on the Southern High and yielded shorter sequences of similar age. Clearly interpretable magnetic stratigraphies were obtained from all sites using the shipboard pass-through magnetometer. These results were augmented using discrete sample cubes (7 cm³) collected shipboard and measured postcruise. Miocene age sediments are separated by a hiatus from Oligocene, Eocene, and Cretaceous age sediments beneath. An astrochronological age model was developed for the six sites based on cycles observed in reflectance data, measured shipboard. This age model is in good agreement with published astrochronological polarity chron ages in the 1- to 6-Ma interval.

¹Evans, H.F., Channell, J.E.T., and Sager, W.W., 2005. Late Miocene–Holocene magnetic polarity stratigraphy and astrochronology, ODP Leg 198, Shatsky Rise. In Bralower, T.J., Premoli Silva, I., and Malone, M.J. (Eds.), *Proc. ODP, Sci. Results*, 198, 1–39 [Online]. Available from World Wide Web: <http://www-odp.tamu.edu/publications/198_SR/VOLUME/CHAPTERS/118.PDF>. [Cited YYYY-MM-DD]

²Department of Geological Sciences, University of Florida, Gainesville FL 32611, USA. Correspondence author: geohelen@ufl.edu

³Department of Oceanography, Texas A&M University, College Station TX 77843, USA.

INTRODUCTION

Shatsky Rise is a medium-sized large igneous province in the west-Central Pacific Ocean (Fig. F1) and is possibly the oldest existing oceanic plateau. The rise consists of three prominent topographic highs. Sites 1209, 1210, 1211, and 1212 were cored on the Southern High (Bralower, Premoli Silva, Malone, et al., 2002). Eight sites on the Southern High of the rise were drilled during Deep Sea Drilling Project (DSDP) and earlier Ocean Drilling Program (ODP) legs (Sites 47, 48, 49, 50, 305, 306, 577, and 810). Of these, ODP Sites 577 and 810 provided interpretable Neogene magnetic stratigraphies.

Sites 1207 and 1208, from the Northern and Central Highs, provided unexpectedly expanded late Miocene (12.5 Ma) to Holocene sequences. These locations had not been cored during previous DSDP/ODP expeditions. The initial age model for all of the sites was based on correlation of the sequence of polarity zones to the geomagnetic polarity timescale (GPTS) (Cande and Kent, 1992, 1995). Mean sedimentation rates at the five sites vary from 1 to 4 cm/k.y. Latitude and longitude of the sites and basal ages of the Neogene sediments are given in Table T1. Neogene sediments at the sites consisted mostly of light gray to pale orange nannofossil oozes with varying amounts of clay, radiolarians, and diatoms. Magnetic susceptibility is low ($<2 \times 10^{-5}$ SI) at all the sites and shows a decreasing trend from the Quaternary to the late Miocene. Composite sections were constructed shipboard for four of the sites (1209, 1210, 1211, and 1212) using multisensor track (MST) data including magnetic susceptibility and gamma ray attenuation (GRA) bulk density and also reflectance data. Sites 1207 and 1208 were not double-cored, and depths at these sites are in meters below seafloor (mbsf). The magnetic stratigraphy from the six sites (1207–1212) was based on shipboard pass-through magnetometer measurements and discrete samples measured postcruise.

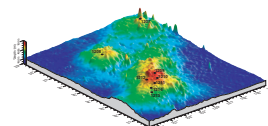
Sediments from five of the sites (1207–1211) showed a prominent cyclicity in reflectance data for parts of the sections, and this is the basis for the construction of an astronomically tuned age model for the 0- to 8-Ma interval. The astronomically calibrated polarity timescale has been well established for the 0- to 6-Ma interval (Shackleton et al., 1990, 1995; Hilgen 1991a, 1991b). Hilgen (1991a, 1991b) produced his astronomically calibrated polarity timescale for the 2- to 5.23-Ma interval using sapropel occurrences and carbonate content in Mediterranean sections. These polarity chron ages were incorporated into the GPTS of Cande and Kent (1995).

In this study we produced an astronomically calibrated magnetic reversal stratigraphy for the 0- to 8-Ma interval. This is in good agreement with Hilgen (1991a, 1991b) and Shackleton et al. (1995) in the 0- to 6-Ma interval. In the 6- to 8-Ma interval, polarity chron ages are in better agreement with the Shackleton et al. (1995) timescale, differing by up to ~200 k.y. from that of Hilgen et al. (1995) and the new Astronomically Tuned Neogene Time Scale (ATNTS2004) of Lourens et al. (in press).

METHODS

Two types of paleomagnetic measurements were made on sediments collected during ODP Leg 198; pass-through measurements on half-

F1. Bathymetric map of Shatsky Rise, p. 10.



T1. Oldest Neogene magnetic polarity chron identified, p. 27.

cores and discrete sample measurements. Discrete sample cubes ($2\text{ cm} \times 2\text{ cm}$) were collected during Leg 198 to augment measurements using the shipboard pass-through magnetometer. Shipboard measurements on half-cores were made at 5-cm intervals. A total of 747 discrete samples were taken at 50-cm intervals. Discrete samples were collected from the center of the half-cores to avoid deformation at the outer edges of the core. Magnetic measurements on the cubes were performed in the magnetically shielded room at the University of Florida (USA) using a 2G Enterprises cryogenic magnetometer. The samples were step-wise alternating-field (AF) demagnetized using a D-Tech D2000 AF demagnetizer. Magnetization component directions were determined using the method of Kirschvink (1980), applied to the 20- to 60-mT peak field demagnetization interval.

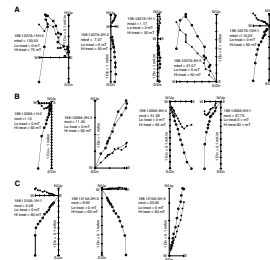
The astrochronology developed for Sites 1207–1211 was based on cycles seen in reflectance data (L^*) measured shipboard on a purpose-built track. Reflectance of visible light from soft-sediment cores was measured using a spectrophotometer at 2.5-cm intervals and provided a high-resolution record of color variations for visible wavelengths (400–700 nm). L^* reflectance represents “lightness” of the sediment, which is usually controlled by changes in percent carbonate.

The initial age model for each site was based on correlation of the polarity zone sequence to the timescale of Cande and Kent (1995). Power spectra using the Blackman-Tukey method with a Bartlett window from the Analyseries software of Paillard et al. (1996) indicate the presence of obliquity and eccentricity peaks. The reflectance data were then tuned to the astronomic solutions for obliquity from Laskar et al. (1993). This allowed astronomically calibrated ages to be assigned to the polarity reversal boundaries at Sites 1207–1211. Site 1212 was not included in the astrochronology, as it contains a hiatus at 4–5 Ma.

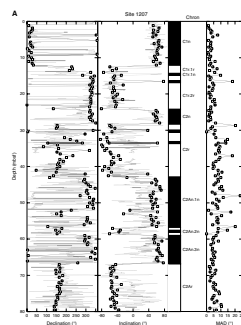
MAGNETOSTRATIGRAPHIC INTERPRETATION

Site 1207 is the only site that has been drilled on the Northern High of Shatsky Rise. The sediment recovered was mostly Neogene in age (0–163.8 mbsf) underlain by Campanian and older oozes and cherts. The sediment consists of nannofossil ooze with diatoms, radiolarians, and clay in varying amounts (Bralower, Premoli Silva, Malone, et al., 2002). The samples taken for paleomagnetic analysis were AF demagnetized in 5-mT steps up to either 50, 60, or 70 mT, depending on the intensity of the natural remanent magnetization (NRM). Less than 10% of the NRM remains after demagnetization at these peak fields, indicating a low-coercivity remanence carrier, most likely magnetite. Orthogonal projections of demagnetization data (Fig. F2A) show well-defined components for most of the Neogene section after removal of the steep drilling-related overprint at peak AF fields of 20 mT. Maximum angular deviation (MAD) values are low for most of the section ($<10^\circ$), indicating well-defined characteristic magnetization components; however, some intervals, particularly the interval between 50 and 60 mbsf (Fig. F3A), have slightly higher MAD values and less well defined components. The interpretation of the magnetic stratigraphy from shipboard and discrete sample data can be accomplished by polarity zone pattern fit to the GPTS (Cande and Kent, 1992, 1995) (Table T2). This pattern fit is satisfactory to the base of Subchron C5An.1n (Fig. F3A, F3B). Below the polarity zone equivalent to Subchron C5An.1n, recovery was intermittent and biostratigraphy indicates a hiatus with Campanian age sed-

F2. Orthogonal projections of AF demagnetization, p. 11.



F3. Component inclination and declination, Site 1207, p. 13.



T2. Magnetostratigraphic age model, p. 28.

iments below (Bralower, Premoli Silva, Malone, et al., 2002). Sedimentation rates average 1–2 cm/k.y. throughout the section with some slightly higher (3–4 cm/k.y.) rates in the Late Pliocene and late Miocene (Fig. F4A). Component declination has been corrected for each core using Tensor orientation data measured shipboard. The mean inclination in normal polarity zones for the site is 57.8° , close to the expected inclination of 56° for a geocentric axial dipole at this site; however, reversed polarity intervals have a mean inclination of -51.1° , shallower than expected. This can be attributed to shallowing of reversed polarity directions by the steep downward-directed drilling overprint, shown clearly in the orthogonal projections (Fig. F2A).

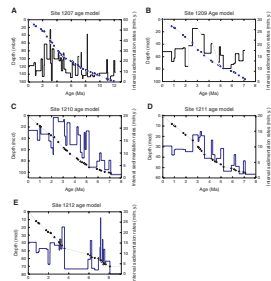
Sites 1209–1212 are located on the Southern High of Shatsky Rise (Fig. F1). Multiple holes were drilled at each site and composite sections were constructed using shipboard MST data. Discrete sample cubes were only collected from Holes 1209A, 1210A, 1211A, and 1212A. Shipboard data from the pass-through magnetometer are consistent between the different holes at each site and confirms the interpretation of the magnetic stratigraphy (see Shipboard Scientific Party, 2002).

As for Site 1207, orthogonal projections from discrete sample data show two components: a steep downward drilling-related overprint and well-defined characteristic components (Fig. F2B, F2C, F2D, F2E). In most cases the drilling-related overprint was easily removed in peak AF fields of 10–20 mT. Little of the NRM remained at peak fields of 60 mT. MAD values are generally $<5^\circ$ throughout the sections. The expected inclination for the Southern Rise is 51° ; again, all the sites show slightly steeper than expected inclinations in normal polarity zones and shallower than expected inclination in reversed polarity zones. The magnetostratigraphic age models indicate mean sedimentation rates between 1 and 3 cm/k.y. for most of the Neogene (Fig. F2B, F2C, F2D, F2E).

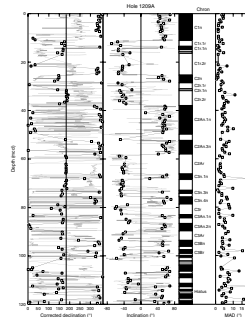
The polarity interpretation at Sites 1209, 1210, and 1211 is unambiguous back to Subchron C3Bn (Table T2; Figs. F5, F6, F7). Below this level, interpretation becomes difficult due to decreasing sedimentation rates leading to a hiatus recognized at all sites between the upper Miocene and Oligocene and older sequences. At Site 1212, a hiatus accounts for the interval between 4 and 5 Ma (Chron C3), and the polarity interpretation can be accomplished to Subchron C4n.2n (Fig. F8). This interpretation of the sequence of polarity zones is confirmed by shipboard biostratigraphy. The interpretation of the polarity stratigraphy was carried out using data measured shipboard augmented with discrete sample cubes. When the magnetostratigraphic data were placed on the composite depth scale, the reversal boundaries were found to be consistent between holes, indicating that there is very little error in the depths of polarity zone boundaries or in composite depth calculations. The magnetic measurements made shipboard do include a small amount of error due to the response function of the shipboard magnetometer. The response function of the wide-access magnetometer used to measure half-cores is ~ 10 cm, resulting in a centimeter-scale uncertainty in the placement of the reversal boundaries.

Site 1208 is located on the Central High of Shatsky Rise and also provided an expanded late Miocene–Holocene section. The magnetic stratigraphy from Site 1208 will be presented elsewhere (Evans et al., unpubl. data).

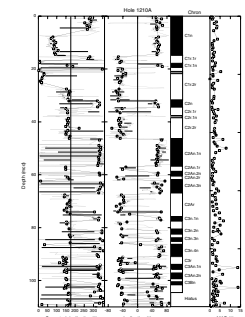
F4. Age model and sedimentation rates, p. 15.



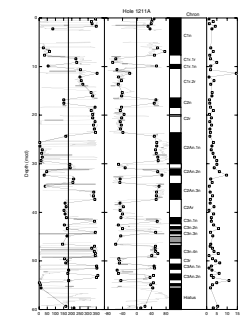
F5. Component inclination and declination, Site 1209, p. 16.



F6. Component inclination and declination, Site 1210, p. 17.



F7. Component inclination and declination, Site 1211, p. 18.



ASTROCHRONOLOGY

Cycles were visually identifiable in L^* reflectance data from all five of the sites in this study. For Sites 1209, 1210, and 1211, we worked with spliced composite records rather than data from a single hole. Reflectance data were initially placed on the magnetostratigraphic age model based on the polarity timescale of Cande and Kent (1995). Power spectra for untuned sections of reflectance data placed on this age model consistently show a concentration of power at orbital frequencies, particularly around the 41-k.y. obliquity cycle (Fig. F9).

The reflectance records were then tuned to the astronomical solution for obliquity from Laskar et al. (1993), as this was the most visually identifiable cycle in the reflectance data and the power spectra for different time intervals in all the sites showed a concentration of power at the obliquity frequency (Fig. F9). In constructing the astrochronological age model, we assume that there was no phase lag between the orbital forcing and the response. For convenience, the reflectance data were broken up into 1-m.y. intervals when compared to the astronomical solution and each site was tuned independently. Cycles were readily apparent in the reflectance data for all sites, and tuning of the record required a minimum of adjustment of peaks in the reflectance data to the astronomical solution (Figs. F10, F11, F12, F13). Astronomically tuned ages were calculated for polarity reversals in the 1- to 8-Ma interval at Site 1207 (Table T3). At Site 1209, tuning was performed in the 1- to 7-Ma interval and at Sites 1210 and 1211 in the 1- to 5-Ma interval. Site 1208 has also provided an astrochronological age model for the 1- to 6-Ma interval (Fig. F11) and is included in Table T3. The tuned age models are compared to each other (Table T3) and are compared with other recently published astrochronologies for this time period (Table T4). The output of a bandpass filter centered on 41 k.y. is shown below the astronomical solution for obliquity and the raw reflectance data in Figures F10, F11, F12, F13, and F14.

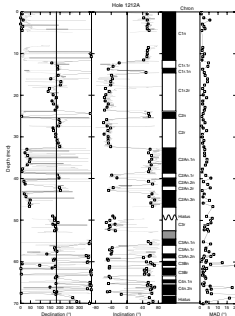
To test the validity of the timescale we used cross-spectral analysis performed using the Blackman-Tukey method and Analyseries software (Paillard et al., 1996). Coherence between the reflectance data and the astronomical solution for obliquity was significant at all the sites, although the coherence values depend on which time interval is being examined. At Site 1207 coherence was ~0.8 for the 1.2- to 1.8-Ma and 6.2- to 6.8-Ma intervals (Fig. F15A). The coherence values at Site 1208 were >0.8 for the entire 1-to 6-Ma interval. Sites 1209, 1210, and 1211 also showed coherence values between 0.8 and 1 (Fig. F15C–F15E).

DISCUSSION

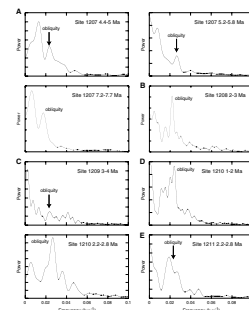
Comparison of the tuned ages for polarity reversal boundaries at the five sites in the 1.5- to 2-Ma interval showed that polarity chron ages are in good agreement. For other time intervals there are some significant differences (more than an obliquity cycle) between sites (Table T3). Intervals with enhanced 41-k.y. power in reflectance data are considered more reliable (bold in Table T3). Site 1208 showed the strongest cyclicity, with Site 1207 also showing a clear signal in some intervals, particularly the 2.1- to 2.7-Ma and 4.5- to 5-Ma intervals.

During ODP Leg 138 to the eastern equatorial Pacific, 11 sites were drilled and most of them showed a prominent cyclicity in GRA density. Shackleton et al. (1995) used these cycles in GRA density records to pro-

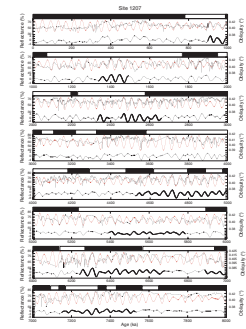
F8. Component inclination and declination, Site 1212, p. 19.



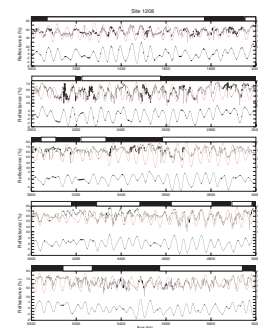
F9. Power spectra, p. 20.



F10. Astronomical obliquity vs. tuned L^* , Site 1207, p. 21.



F11. Astronomical obliquity vs. tuned L^* , Site 1208, p. 22.

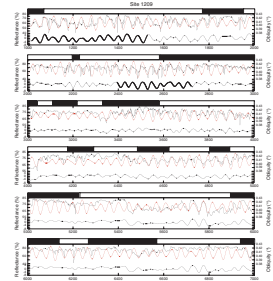


duce an orbitally tuned age model for the 0- to 12.5-Ma interval. They worked entirely in the time domain comparing smoothed GRA density records with the target record of summer insolation at 65°N. In their tuning they assumed that no phase lag existed between insolation and GRA density controlled by proportion of SiO₂ and CaCO₃ (high density), high carbonate content being associated with high Northern Hemisphere insolation. Age control points were added to the data to align prominent groups of density maxima. The records were broken into 0.8-m.y. intervals for convenient viewing. Each site was tuned independently over the chosen time interval. Shackleton et al. (1995) found that some intervals in these records were more easily tuned than others, similar to results from Leg 198. Shackleton et al. (1995) noted that it was difficult to tune the 0- to 1-Ma interval, which was also the case at four of the Leg 198 Sites (1208, 1209, 1210, and 1211). The 1- to 2-Ma interval for the Leg 138 sites carries a clear 41-k.y. obliquity cycle. For Leg 198 sites, the 1.2- to 1.6-Ma interval also carries a very clear obliquity cycle (Figs. F10, F11, F12, F13, F14). In the 2.4- to 2.6-Ma interval, a very strong obliquity cycle was observed at Site 846 (Leg 138), and this same interval also carries a strong 41-k.y. signal at Sites 1209, 1210, and 1211. Comparison between the Site 1207 age model and ages from Shackleton et al. (1995) indicate consistency for the 1- to 8-Ma time interval (Table T4).

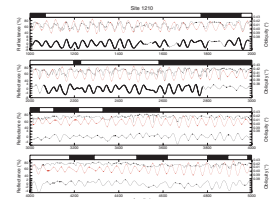
Hilgen et al. (1995) developed an astronomical timescale for the interval from 3 to 9.7 Ma using lithologic cyclicity seen in sedimentary sections in the Mediterranean. These sections comprise open marine sediments that alternate between carbonate-rich and carbonate-poor marls or homogeneous marls and sapropels. The individual sapropels were related to precession minima and the clusters of sapropels to the 400-k.y. eccentricity cycles. In tuning the section, the target curve used was the 65°N summer insolation curve. To obtain an astronomical age for the youngest polarity reversal in the sequence, Hilgen et al. (1995) took the Shackleton et al. (1995) age for the onset of Subchron C3An.2n of 6.576 Ma. They then matched the lithologic cycles in the section to the astronomical solution using the correlation of sapropel clusters to eccentricity. The age of the calibration point (6.576 Ma) had to be adjusted to 100 k.y. older to establish a consistent correlation between sapropel clusters and eccentricity maxima. The ages from Hilgen et al. (1995) differ significantly from those from Leg 198 in the 6- to 8-Ma interval (Table T4). At the top of Subchron C3Bn the difference is >200 k.y. In the interval from 7.2 to 8.1 Ma, the difference is ~100 k.y., which is the amount of adjustment of the 6.576-Ma tie point used by Hilgen et al. (1995) for the age of the youngest polarity reversal in their section.

ODP Site 926 on the Ceara Rise also produced an orbitally tuned timescale from 5 to 14 Ma (Shackleton and Crowhurst, 1997). This timescale cannot be directly compared with the Leg 198 timescale because of a lack of polarity reversals at Site 926. Backman and Raffi (1997) used the cyclostratigraphic age model from Site 926 to calibrate ages of the calcareous nannofossil datums for the late Miocene. These ages were then compared with the biomagnetochronology from Site 853 (ODP Leg 138). The center of the peak in abundance of transitional morphotypes of *Triquetrorhabdulus rugosus* at Site 853 occurred 120–130 k.y. after the corresponding peak at Site 926. The age estimates of Hilgen et al. (1995) were then applied to the Site 853 data and the peak center was found to coincide at Sites 853 and 926. Therefore, Backman

F12. Astronomical obliquity vs. tuned L*, Site 1209, p. 23.

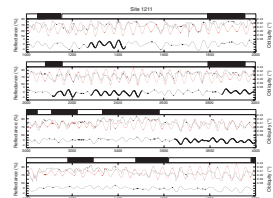


F13. Astronomical obliquity vs. tuned L*, Site 1210, p. 24.

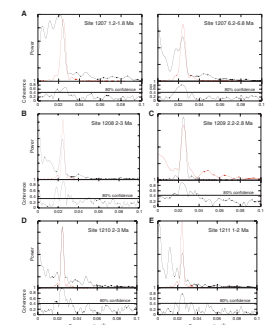


T3. Comparison of astrochronological age models, p. 29.

F14. Astronomical obliquity vs. tuned L*, Site 1211, p. 25.



F15. Cross-spectral analysis, p. 26.



T4. Astrochronological ages for Leg 198, p. 30.

and Raffi (1997) considered that the Hilgen et al. (1995) ages are more reliable in this interval than the ages of Shackleton et al. (1995).

Lourens et al. (in press) recalibrated the Miocene astronomic timescales of Shackleton and Crowhurst (1997) and Hilgen et al. (1995) using the astronomic solution of Laskar et al. (2004). For the last 13 m.y., the retuning resulted in almost negligible changes in the ages of reversal boundaries (Lourens et al. in press). For the 6- to 8-Ma interval, the ATNTS2004 is in close agreement with that of Hilgen et al (1995) and therefore differs significantly from the results of this study.

CONCLUSIONS

Five sites from Shatsky Rise produced high-quality magnetic stratigraphies from the late Miocene to Holocene. Cycles identified in reflectance data from Sites 1207–1211 allowed astronomic calibration of the polarity reversal sequence from ~8 Ma to present. The assumption that there is no phase lag between sedimentary cyclicity and the astronomical parameters allowed the cycles to be tuned to the astronomical solution for obliquity. Cross-spectral analysis on the tuned age model indicated high coherence between the astronomic solution and the reflectance data and confirms the reliability of the tuning. The age model has been compared with other published astrochronologies and is found to be in good agreement with Hilgen (1991a, 1991b) (and, therefore, Cande and Kent [1995]) in the 1- to 6-Ma interval. In the 6- to 8-Ma interval the age model differs significantly from that of Lourens et al. (in press) and Hilgen et al. (1995) from the Mediterranean. It is in better agreement with the ODP Leg 138 timescale of Shackleton et al. (1995) from the Pacific Ocean.

ACKNOWLEDGMENTS

We would like to thank Phil Rumford and Bruce Horan at the Gulf Coast Repository for their assistance with sampling. This research used samples and data from the Ocean Drilling Program (ODP). ODP is sponsored by the National Science Foundation (NSF) and participating countries under management of Joint Oceanographic Institutions (JOI), Inc. This research was funded by a grant from the JOI-U.S. Science Support Program.

REFERENCES

- Backman, J., and Raffi, I., 1997. Calibration of Miocene nannofossil events to orbitally tuned cyclostratigraphies from Ceara Rise. In Shackleton, N.J., Curry, W.B., Richter, C., and Bralower, T.J. (Eds.), *Proc. ODP, Sci. Results*, 154: College Station, TX (Ocean Drilling Program), 83–99.
- Bralower, T.J., Premoli Silva, I., Malone, M.J., et al., 2002. *Proc. ODP, Init. Repts.*, 198 [Online]. Available from World Wide Web: <http://www-odp.tamu.edu/publications/198_IR/198ir.htm>
- Cande, S.C., and Kent, D.V., 1992. A new geomagnetic polarity time scale for the Late Cretaceous and Cenozoic. *J. Geophys. Res.*, 97:13917–13951.
- Cande, S.C., and Kent, D.V., 1995. Revised calibration of the geomagnetic polarity timescale for the Late Cretaceous and Cenozoic. *J. Geophys. Res.*, 100:6093–6095.
- Hilgen, F.J., 1991a. Astronomical calibration of Gauss to Matuyama sapropels in the Mediterranean and implication for the geomagnetic polarity time scale. *Earth Planet. Sci. Lett.*, 104:226–244.
- Hilgen, F.J., 1991b. Extension of the astronomically calibrated (polarity) time scale to the Miocene/Pliocene boundary. *Earth Planet. Sci. Lett.*, 107:349–368.
- Hilgen, F.J., Krijgsman, W., Langereis, C.G., Lourens, L.J., Santarelli, A., and Zachariasse, W.J., 1995. Extending the astronomical (polarity) time scale into the Miocene. *Earth Planet. Sci. Lett.*, 136:495–510.
- Kirschvink, J.L., 1980. The least-squares line and plane and the analysis of palaeomagnetic data. *Geophys. J. R. Astron. Soc.*, 62:699–718.
- Laskar, J., Joutel, F., and Boudin, F., 1993. Orbital, precessional, and insolation quantities for the Earth from -20 Myr to +10 Myr. *Astron. Astrophys.*, 270:522–533.
- Laskar, J., Robutel, P., Joutel, F., Gastineau, M., Correia, A.C.M., and Levrard, B., 2004. A long term numerical solution for the insolation quantities of the Earth. *Astron. Astrophys.*, 428:261–285.
- Lourens, L.J., Hilgen, F.J., Laskar, J., Shackleton, N.J., and Wilson, D., in press. The Neogene period. In Gradstein, F.M., Ogg, J., et al. (Eds.), *A Geological Time Scale 2004*: Cambridge (Cambridge Univ. Press).
- Paillard, D., Labeyrie, L., and Yiou, P., 1996. Macintosh program performs time-series analysis. *Eos, Trans. Am. Geophys. Union*, 77:379.
- Shackleton, N.J., Berger, A., and Peltier, W.A., 1990. An alternative astronomical calibration of the lower Pleistocene timescale based on ODP Site 677. *Trans. R. Soc. Edinburgh: Earth Sci.*, 81:251–261.
- Shackleton, N.J., and Crowhurst, S., 1997. Sediment fluxes based on an orbitally tuned time scale 5 Ma to 14 Ma, Site 926. In Shackleton, N.J., Curry, W.B., Richter, C., and Bralower, T.J. (Eds.), *Proc. ODP, Sci. Results*, 154: College Station, TX (Ocean Drilling Program), 69–82.
- Shackleton, N.J., Crowhurst, S., Hagelberg, T., Pisias, N.G., and Schneider, D.A., 1995. A new late Neogene time scale: application to Leg 138 sites. In Pisias, N.G., Mayer, L.A., Janecek, T.R., Palmer-Julson, A., and van Andel, T.H. (Eds.), *Proc. ODP, Sci. Results*, 138: College Station, TX (Ocean Drilling Program), 73–101.
- Shipboard Scientific Party, 2002. Leg 198 summary. In Bralower, T.J., Premoli Silva, I., Malone, M.J., et al., *Proc. ODP, Init. Repts.*, 198: College Station TX (Ocean Drilling Program), 1–148.

APPENDIX

Paleomagnetic data are presented in Tables **AT1**, **AT2**, **AT3**, **AT4**, and **AT5**.

AT1. Paleomagnetic data, Site 1207, p. 31.

AT2. Paleomagnetic data, Site 1208, p. 34.

AT3. Paleomagnetic data, Site 1209, p. 36.

AT4. Paleomagnetic data, Site 1210, p. 38

AT5. Paleomagnetic data, Site 1211, p. 39.

Figure F1. Bathymetric map of Shatsky Rise showing the location of sites drilled during ODP Leg 198 (from Bralower, Premoli Silva, Malone, et al., 2002).

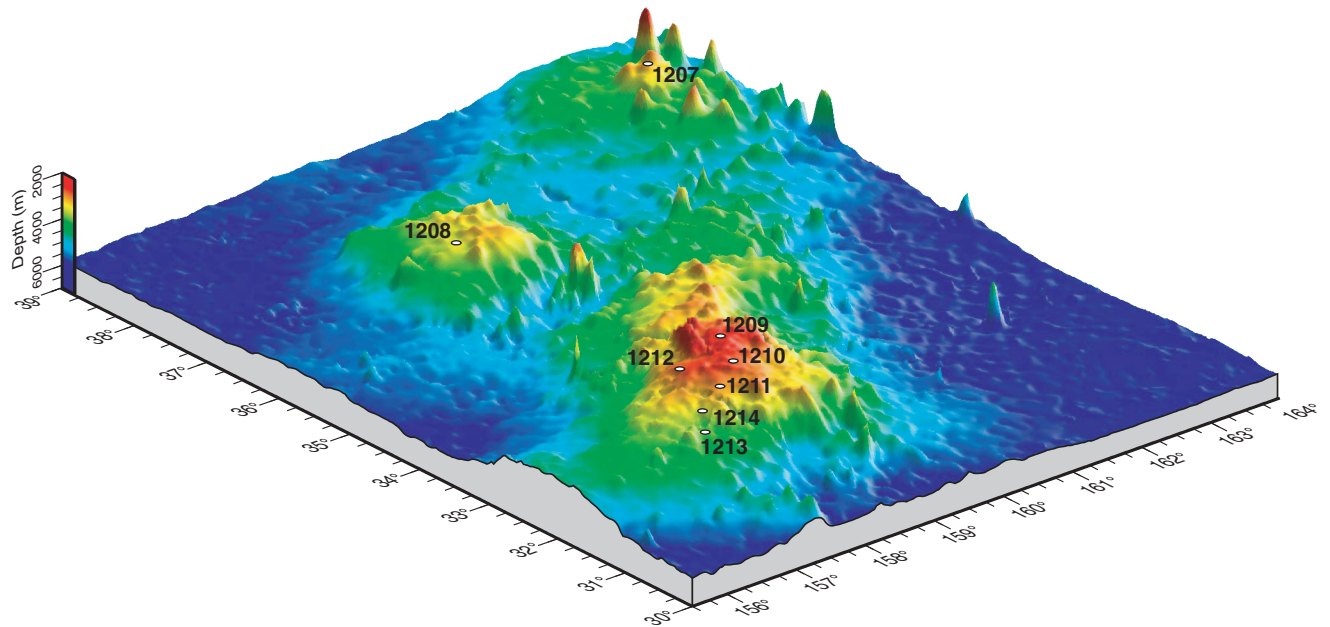


Figure F2. Representative orthogonal projections of AF demagnetization data from (A) Site 1207, (B) Site 1209, (C) Site 1210. Open circles = vector endpoint projection on the vertical plane, solid circles = vector endpoint projection on the horizontal plane. (Continued on next page.)

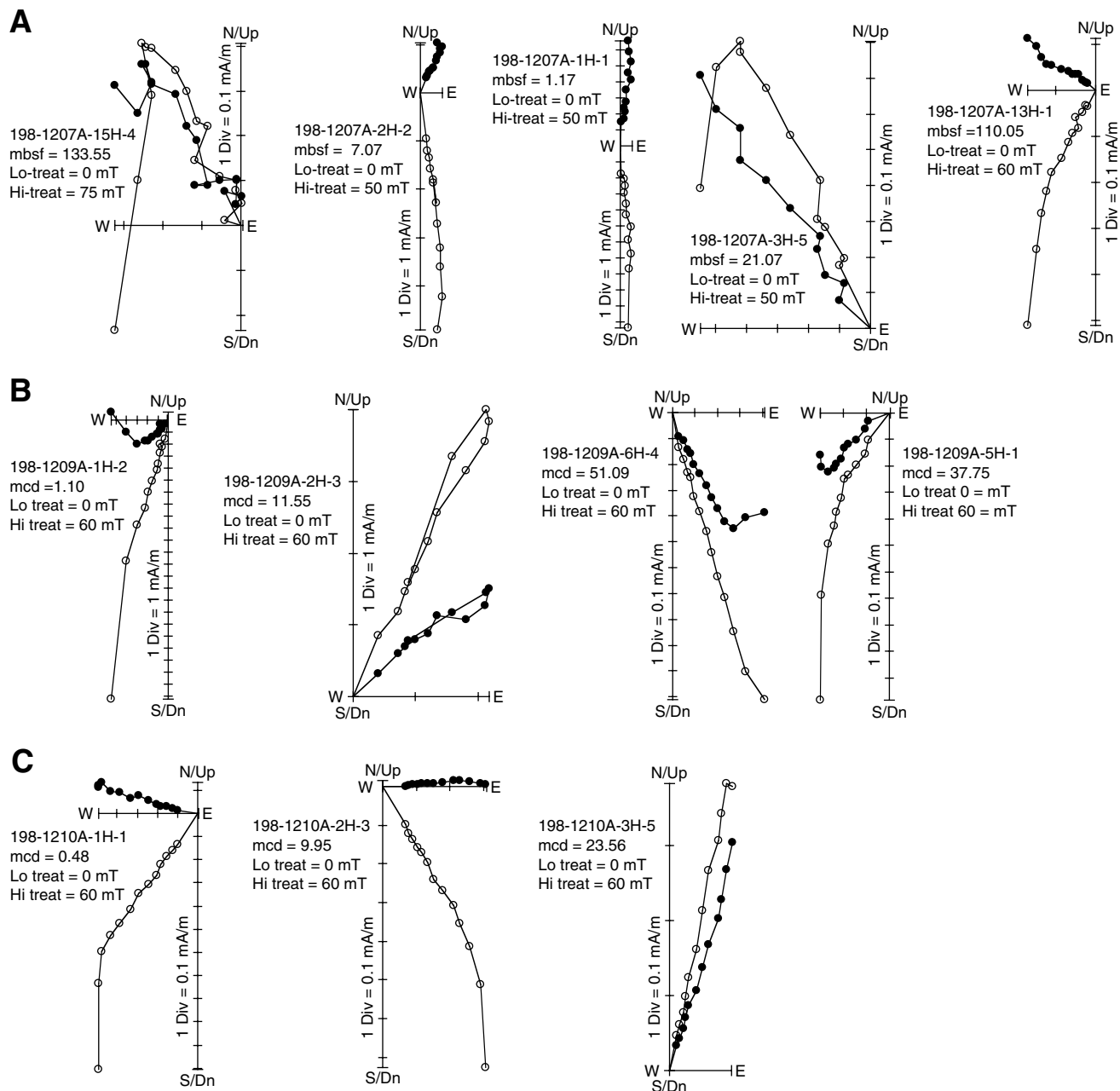


Figure F2 (continued). (D) Site 1211, and (E) Site 1212.

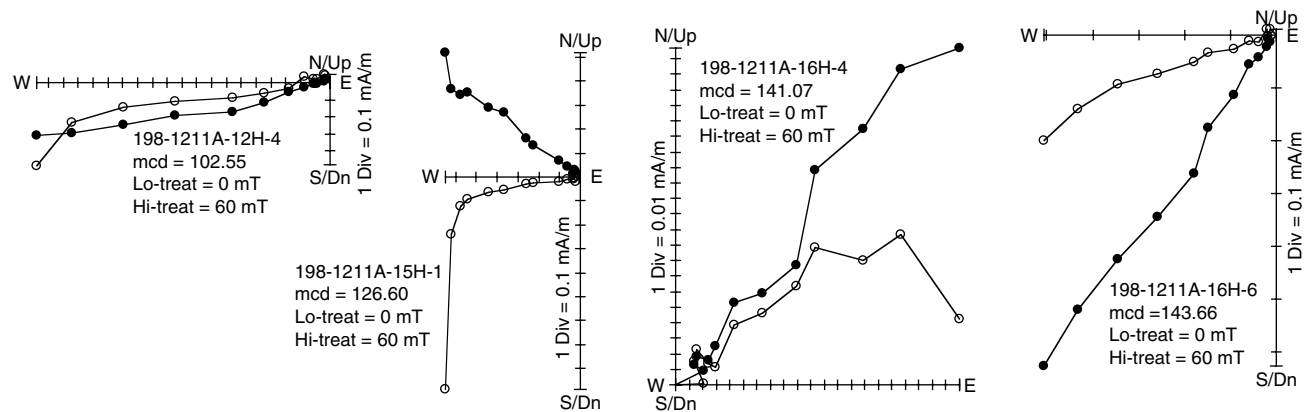
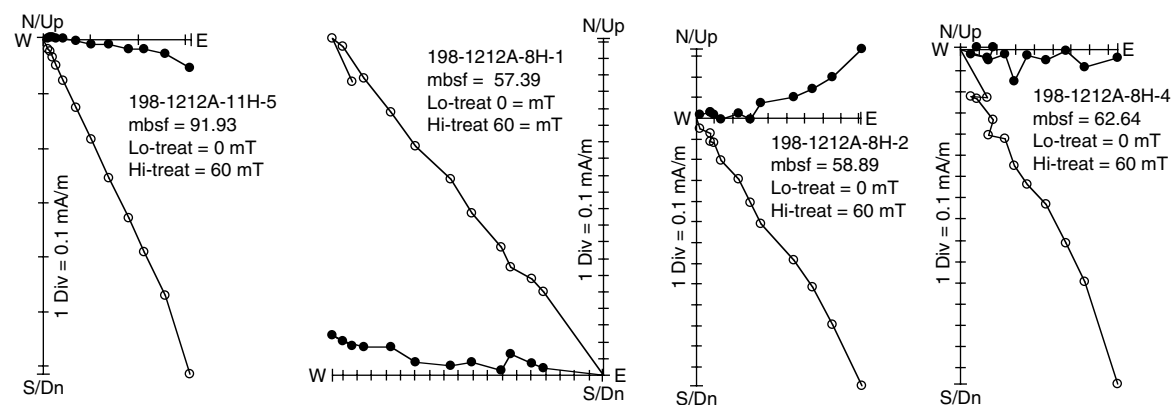
D**E**

Figure F3. A. Site 1207 component inclination and declination from discrete samples (open squares). Inclination and rotated declination from the shipboard pass-through magnetometer after AF demagnetization at peak fields of 20 mT (gray line). Chrons are labeled according to Cande and Kent (1992). Black = normal polarity, white = reversed polarity. Also shown are the maximum angular deviation (MAD) values calculated for discrete sample data (after Kirschvink, 1980). (Continued on next page.)

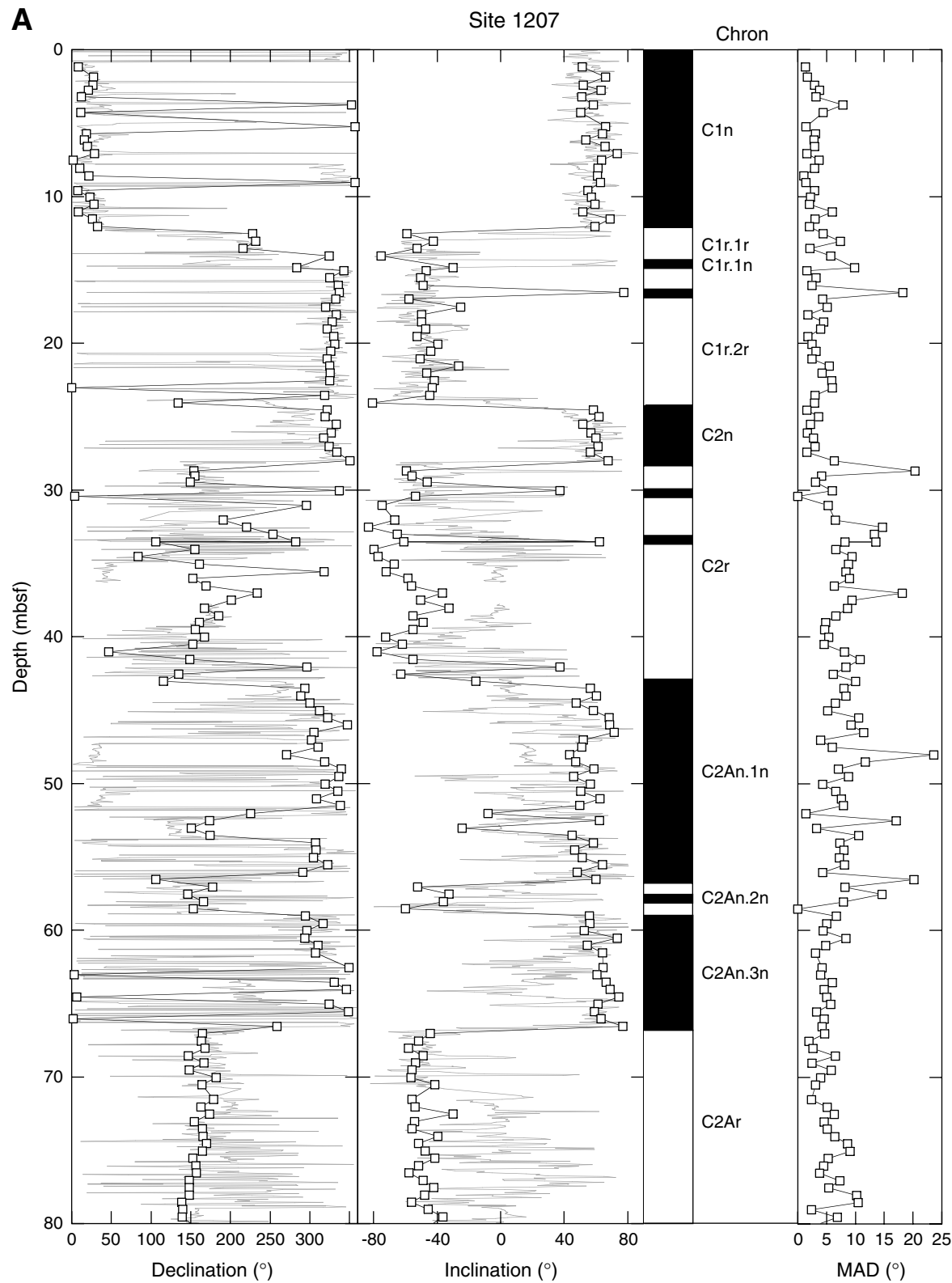


Figure F3 (continued). B. Site 1207 data.

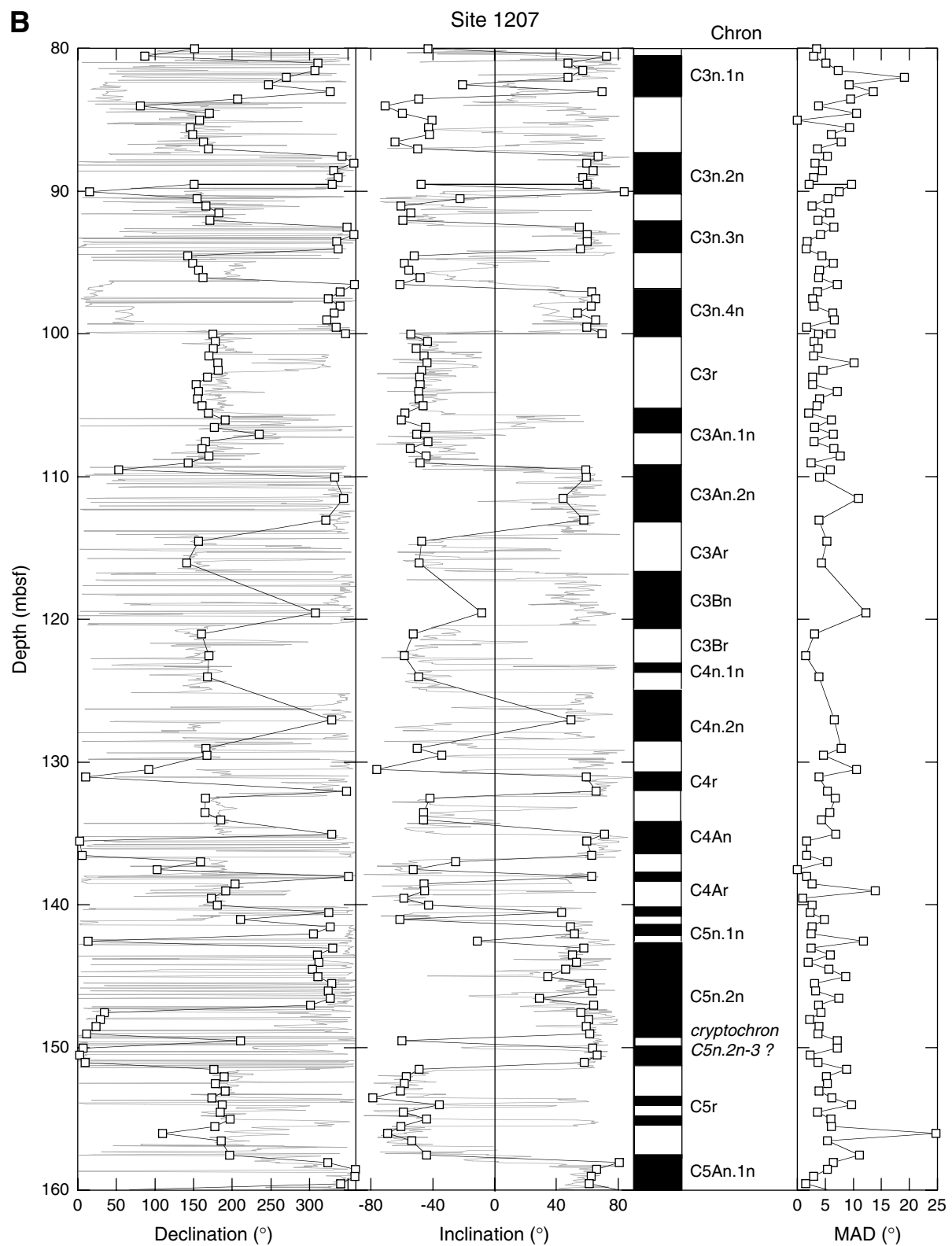


Figure F4. Interval sedimentation rates and age versus depth for the initial age model at (A) Site 1207, (B) Site 1209, (C) Site 1210, (D) Site 1211, and (E) Site 1212.

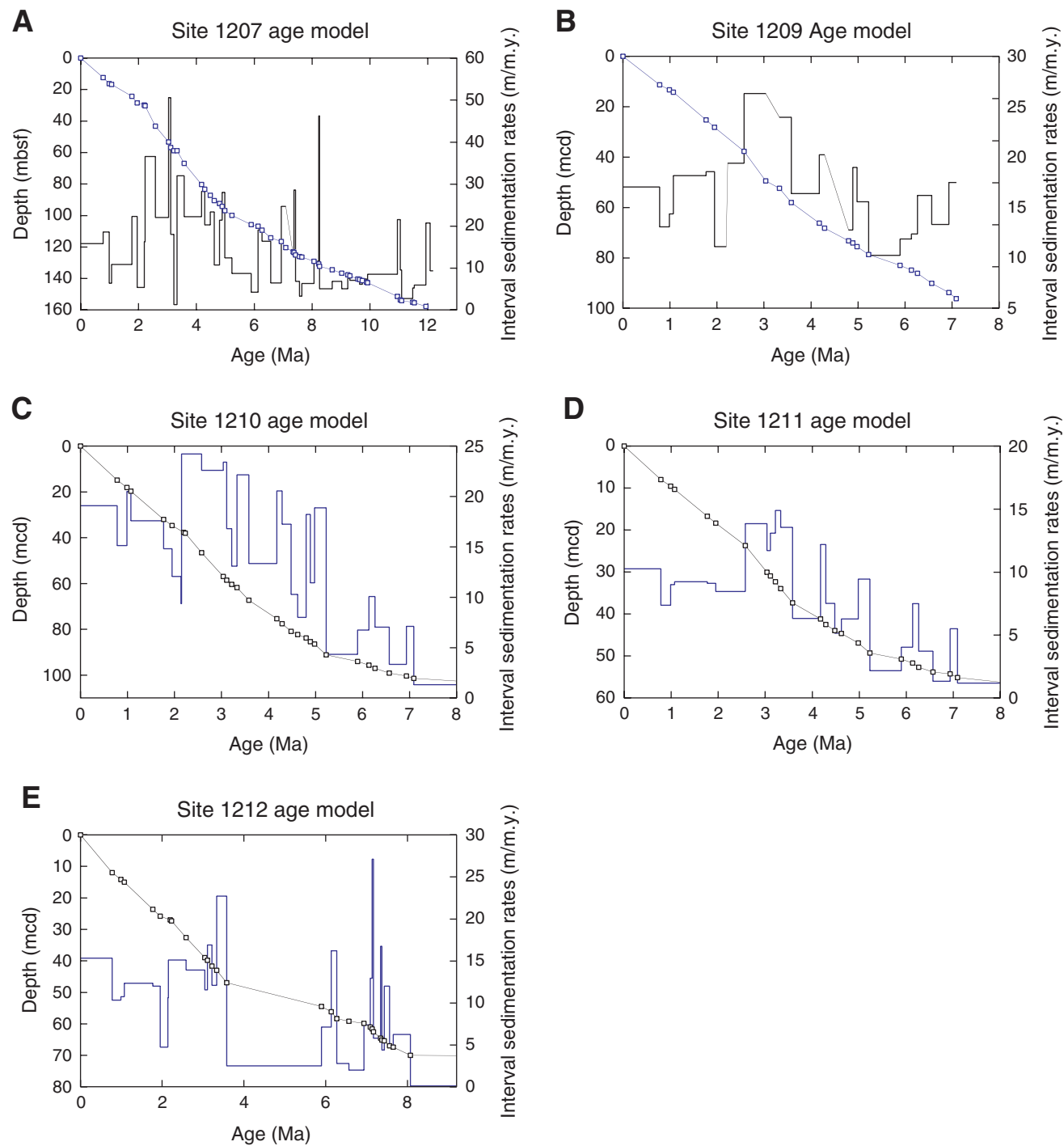


Figure F5. Site 1209 component inclination and declination from discrete samples (open squares). Inclination and rotated declination from the shipboard pass-through magnetometer after AF demagnetization at peak fields of 20 mT (gray line). Chrons are labeled according to Cande and Kent (1992). Black = normal polarity, white = reversed polarity. Also shown are the maximum angular deviation (MAD) values calculated for discrete sample data (after Kirschvink, 1980).

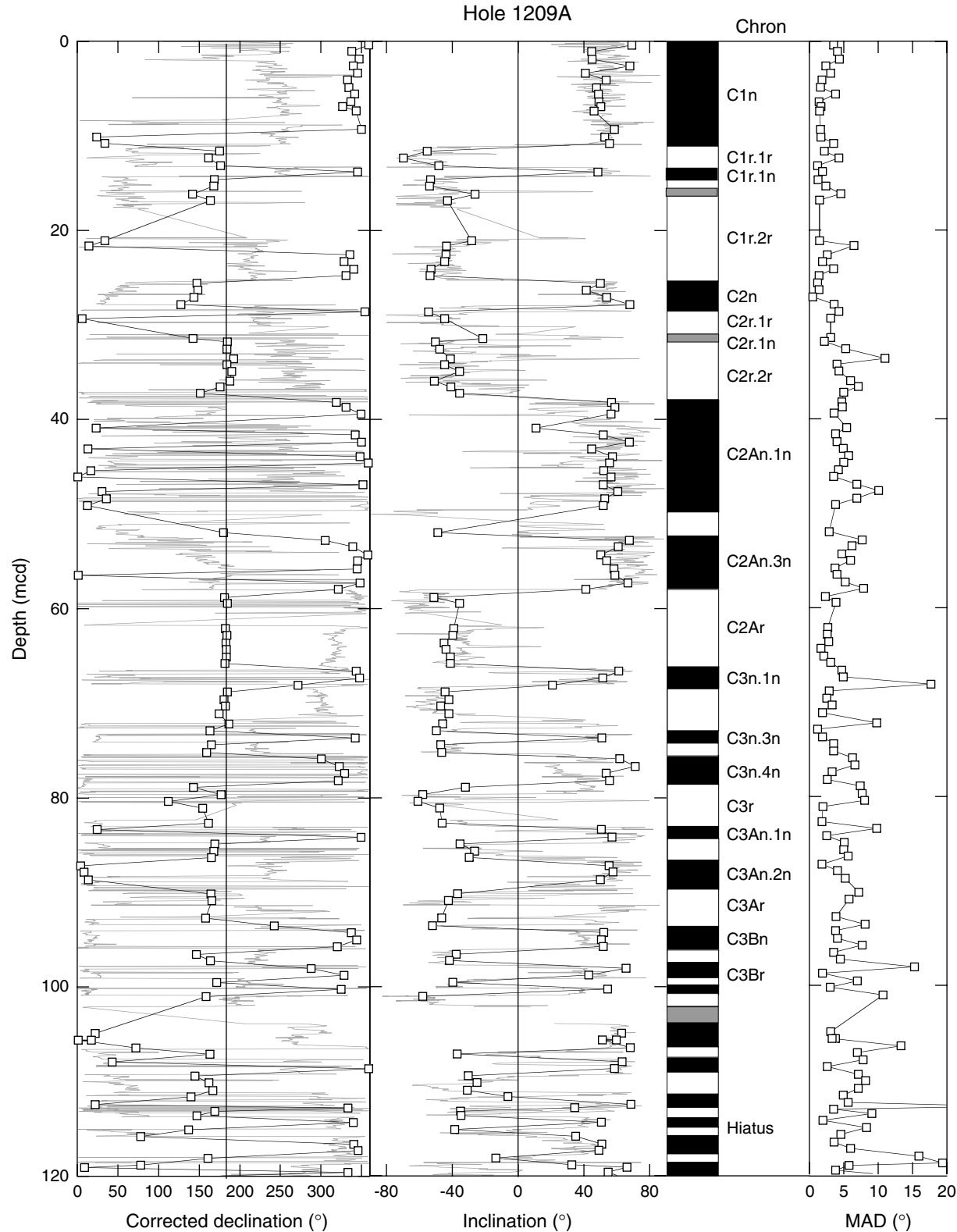


Figure F6. Site 1210 component inclination and declination from discrete samples (open squares). Inclination and rotated declination from the shipboard pass-through magnetometer after AF demagnetization at peak fields of 20 mT (gray line). Chrons are labeled according to Cande and Kent (1992). Black = normal polarity, white = reversed polarity. Also shown are the maximum angular deviation (MAD) values calculated for discrete sample data (after Kirschvink, 1980).

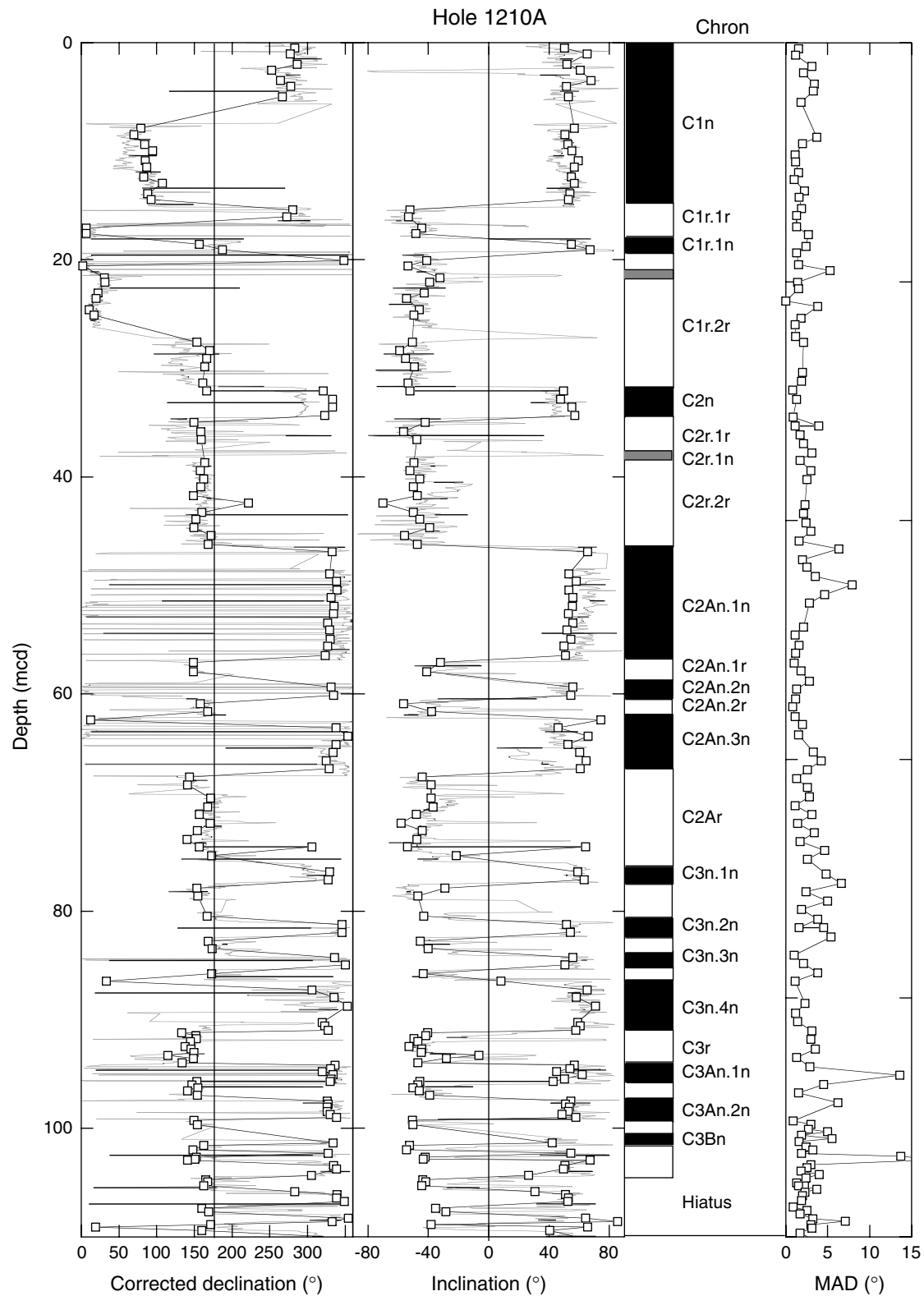


Figure F7. Site 1211 component inclination and declination from discrete samples (open squares). Inclination and rotated declination from the shipboard pass-through magnetometer after AF demagnetization at peak fields of 20 mT (gray line). Chrons are labeled according to Cande and Kent (1992). Black = normal polarity, white = reversed polarity. Also shown are the maximum angular deviation (MAD) values calculated for discrete sample data (after Kirschvink, 1980).

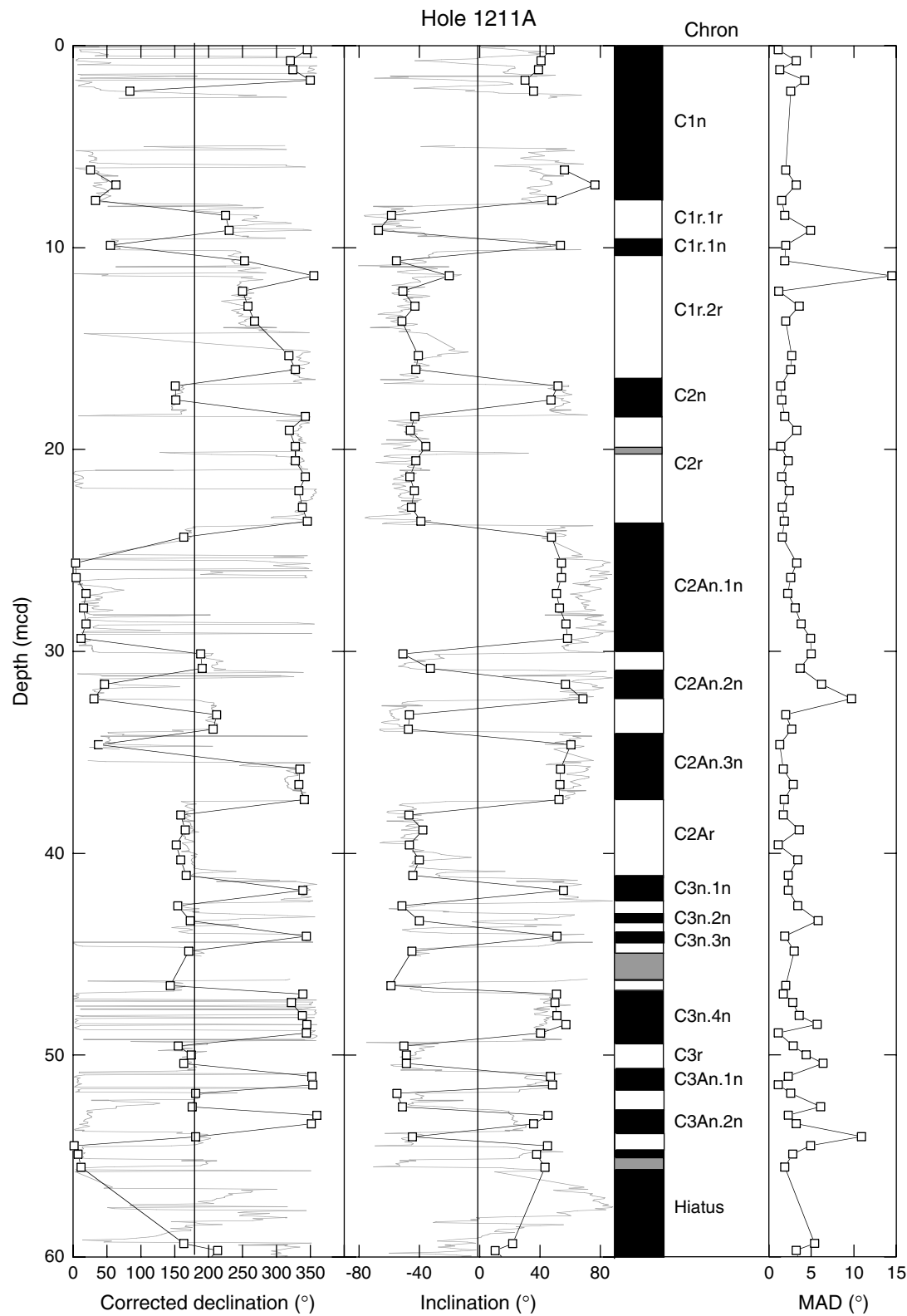


Figure F8. Site 1212 component inclination and declination from discrete samples (open squares). Inclination and rotated declination from the shipboard pass-through magnetometer after AF demagnetization at peak fields of 20 mT (gray line). Chrons are labeled according to Cande and Kent (1992). Black = normal polarity, white = reversed polarity. Also shown are the maximum angular deviation (MAD) values calculated for discrete sample data (after Kirschvink, 1980).

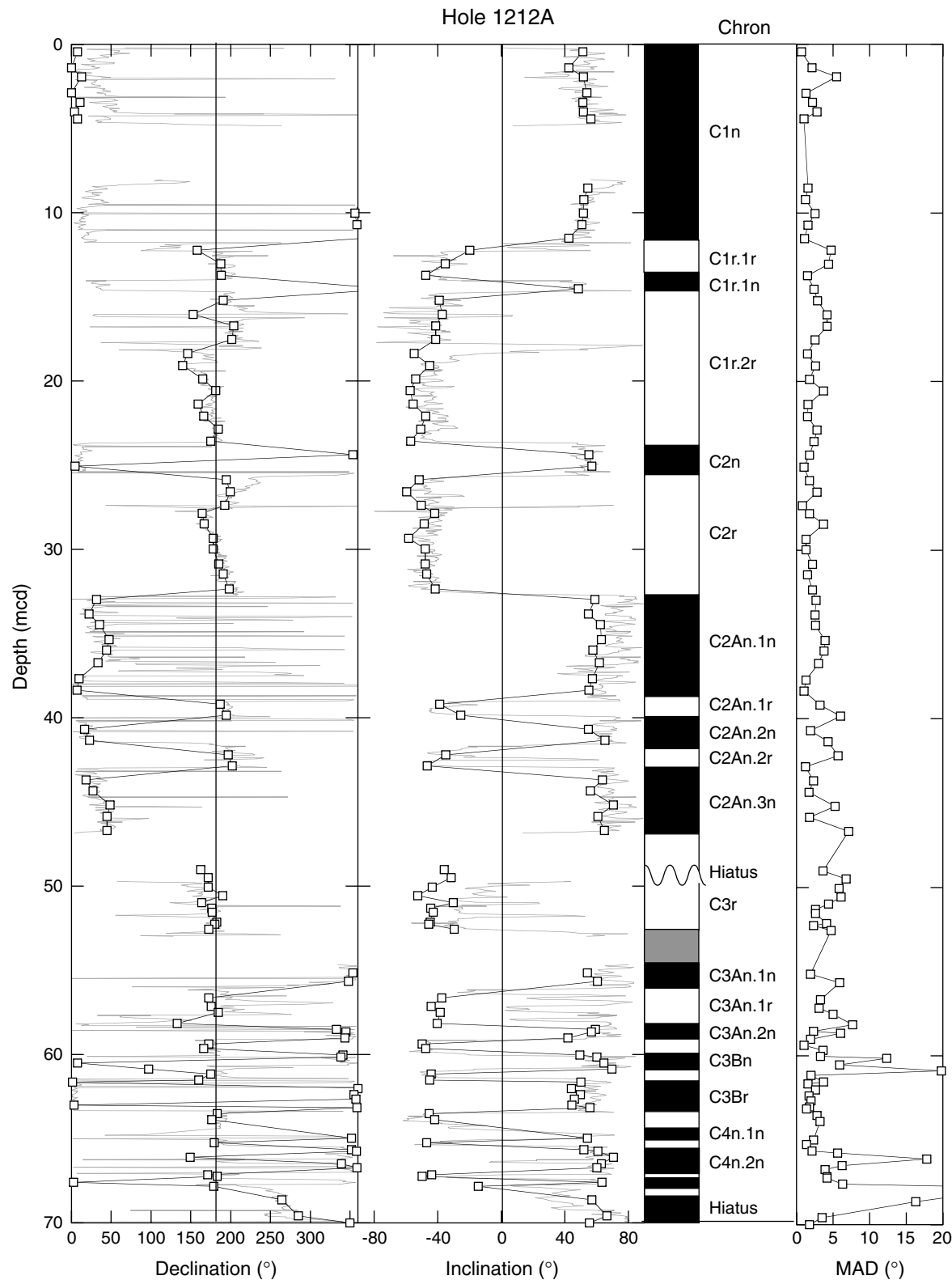


Figure F9. Power spectra from (A) Site 1207, (B) Site 1208, (C) Site 1209, (D) Site 1210, and (E) Site 1211 for reflectance data placed on a Cande and Kent (1995) age model.

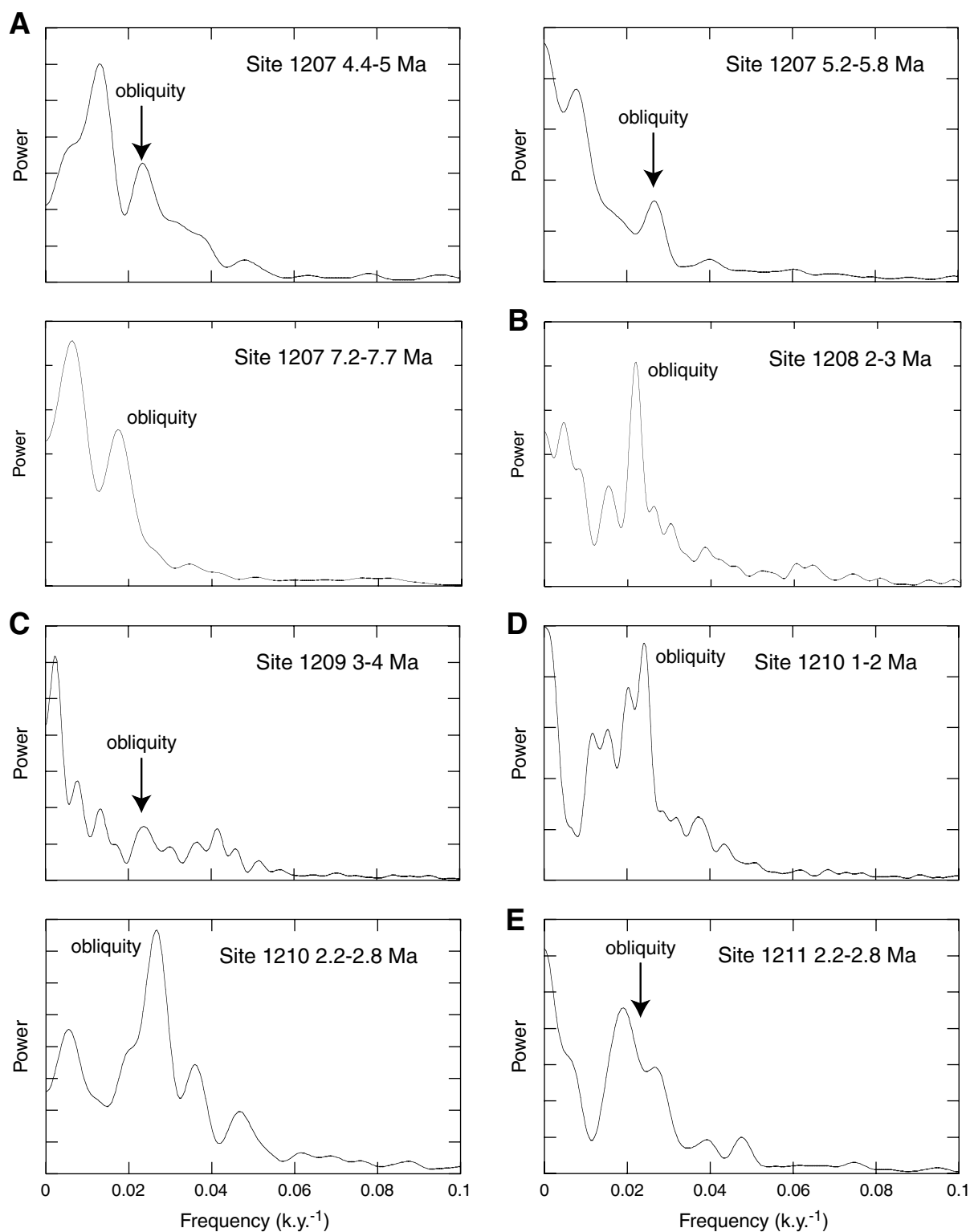


Figure F10. The astronomical solution for obliquity (Laskar, 1993) compared with tuned L* reflectance data from Site 1207 for the 0- to 7-Ma interval. Bandpass-filtered reflectance data centered on 41 k.y. is shown in the lower part of each frame. Black = normal polarity, white = reversed polarity. Heavy line on L* reflectance data indicates intervals where the cyclicity is best developed.

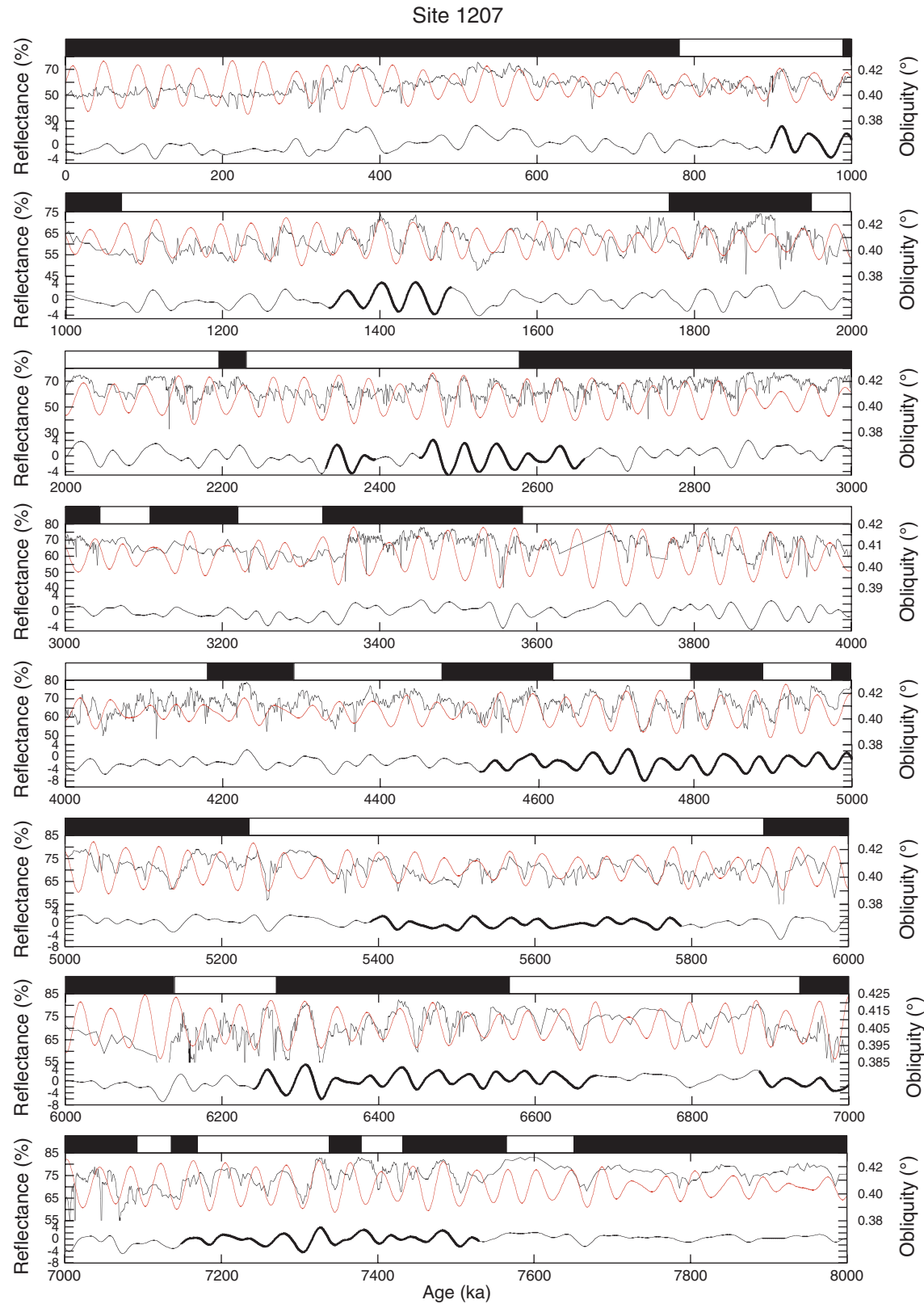


Figure F11. The astronomical solution for obliquity (Laskar, 1993) compared with tuned L* reflectance data from Site 1208 for the 1- to 6-Ma interval. Bandpass-filtered reflectance data centered on 41 k.y. is shown in the lower part of each frame. Black = normal polarity, white = reversed polarity. Heavy line on L* reflectance data indicates intervals where the cyclicity is best developed.

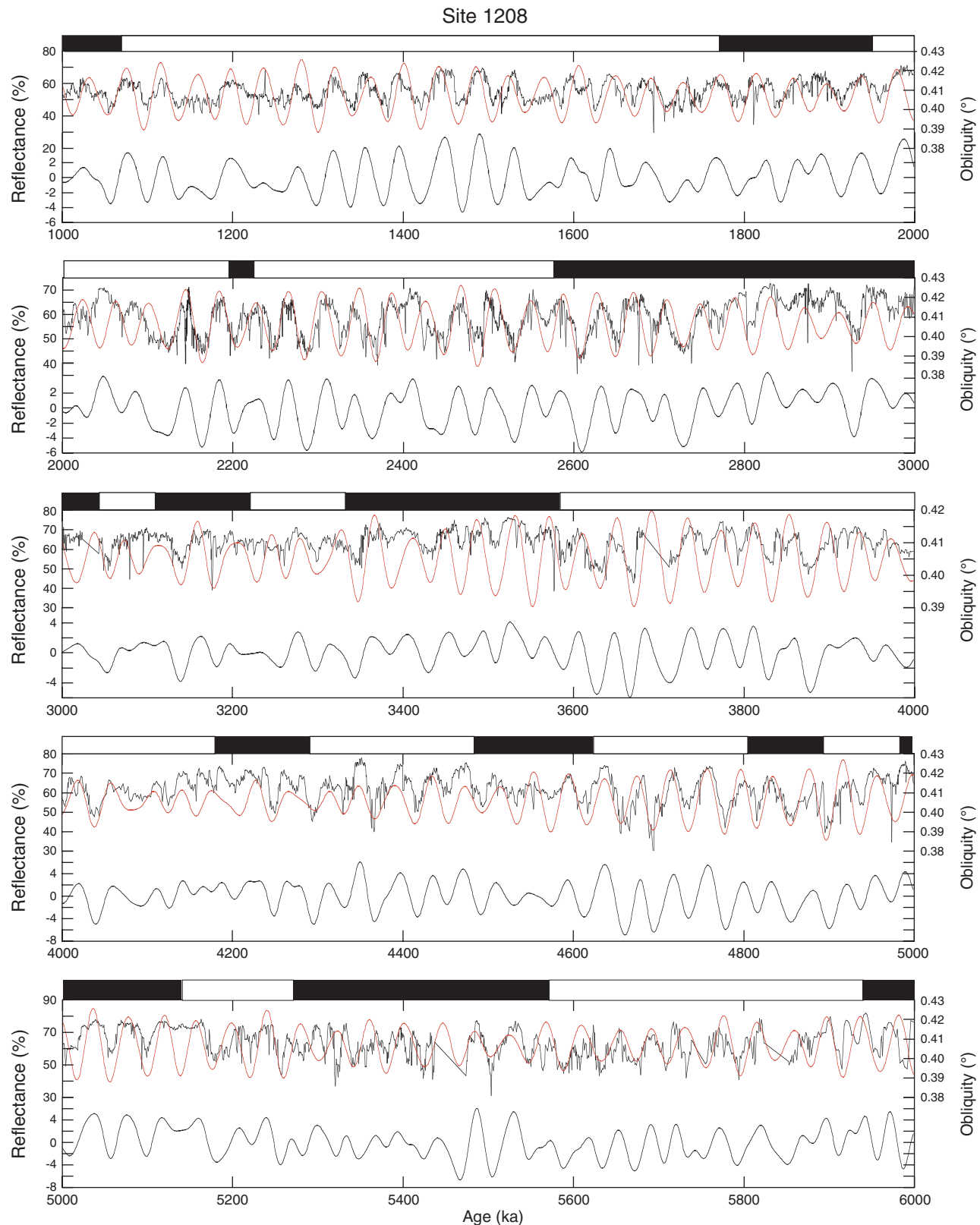


Figure F12. The astronomical solution for obliquity (Laskar, 1993) compared with tuned L* reflectance data from Site 1209 for the 1- to 7-Ma interval. Bandpass-filtered reflectance data centered on 41 k.y. is shown in the lower part of each frame. Black = normal polarity, white = reversed polarity. Heavy line on L* reflectance data indicates intervals where the cyclicity is best developed.

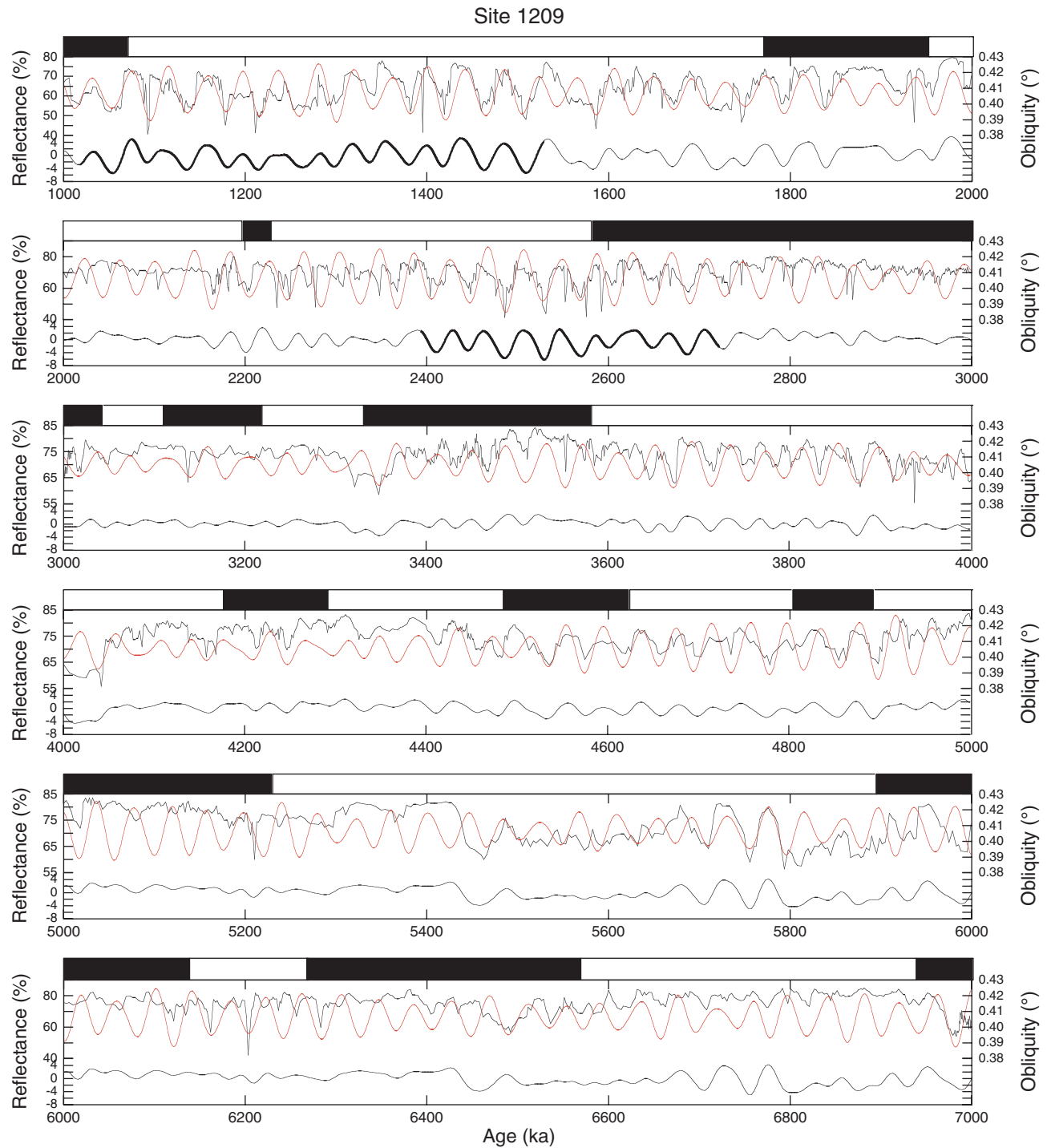


Figure F13. Astronomical solution for obliquity (Laskar, 1993) compared with tuned L* reflectance data from Site 1210 for the 1- to 5-Ma interval. Bandpass-filtered reflectance data centered on 41 k.y. is shown in the lower part of each frame. Black = normal polarity, white = reversed polarity. Heavy line on L* reflectance data indicates intervals where the cyclicity is best developed.

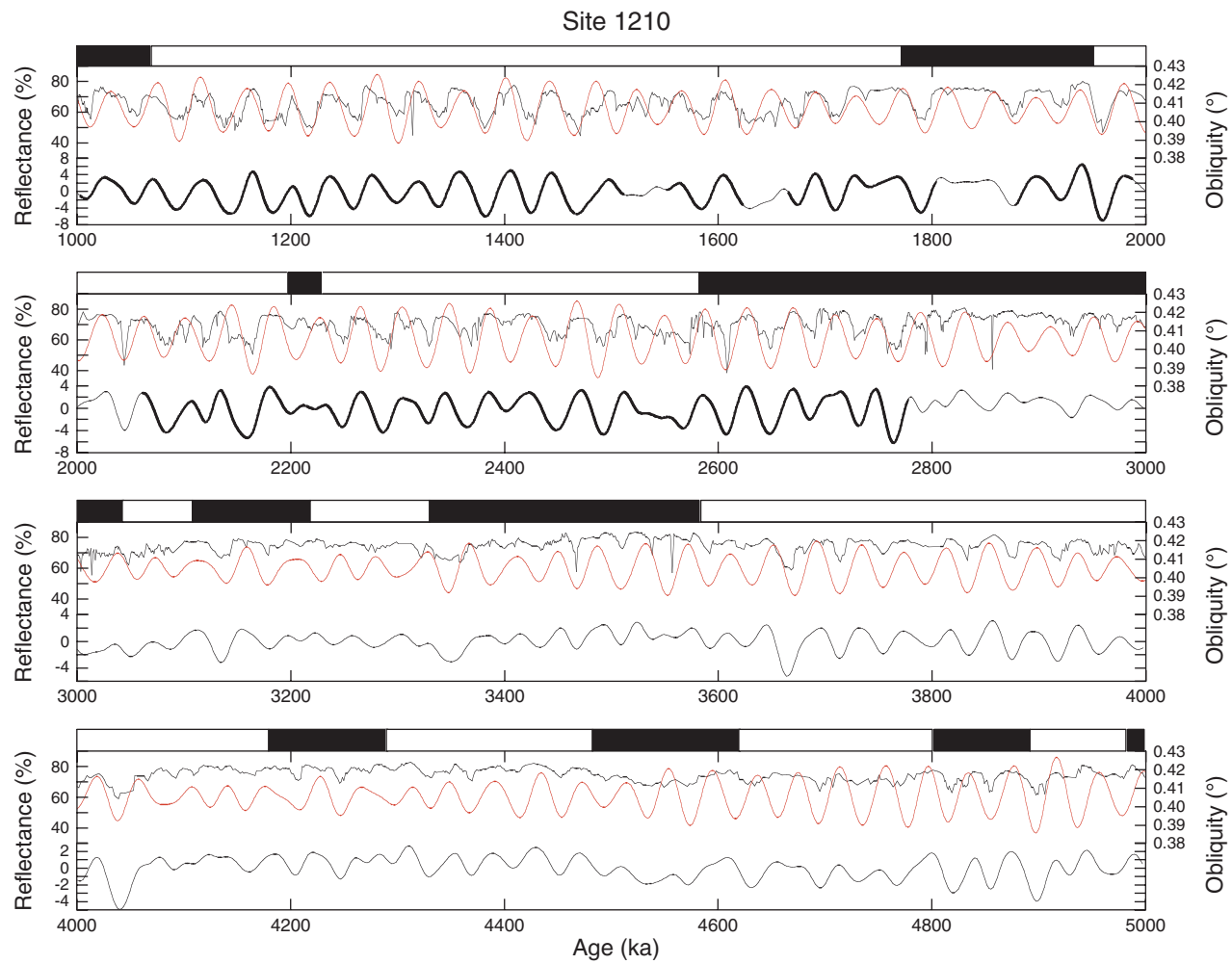


Figure F14. The astronomical solution for obliquity (Laskar, 1993) compared with tuned L* reflectance data from Site 1211 for the 1-5 Ma interval. Bandpass-filtered reflectance data centered on 41 k.y. is shown in the lower part of each frame. Black = normal polarity, white = reversed polarity. Heavy line on L* reflectance data indicates intervals where the cyclicity is best developed.

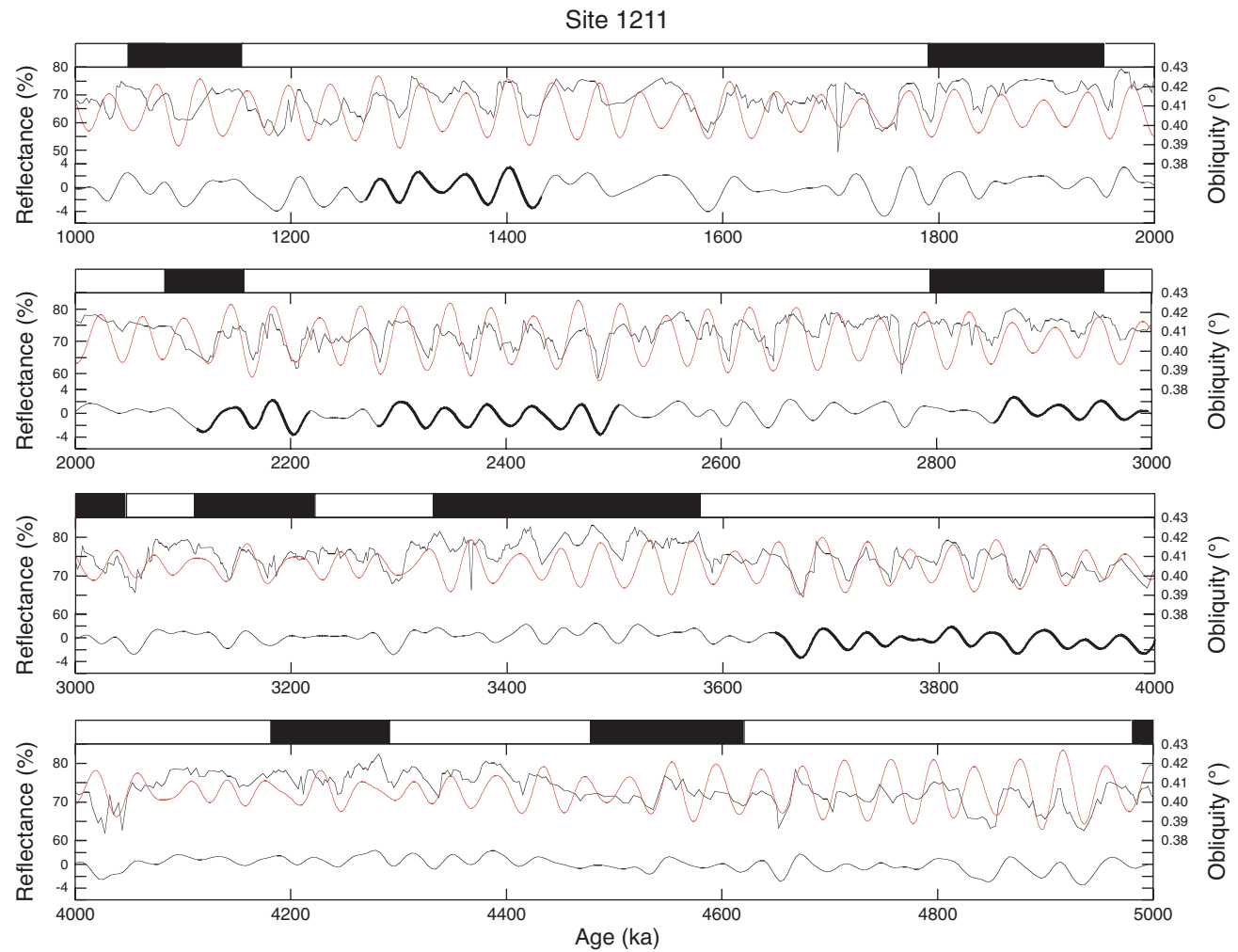


Figure F15. Cross-spectral analysis from (A) Site 1207, (B) Site 1208, (C) Site 1209, (D) Site 1210, and (E) Site 1211. Power spectra are shown for the tuned reflectance data (black) and for the astronomical solution for eccentricity and obliquity (red). Coherence values between the astronomical solutions and reflectance data are shown below.

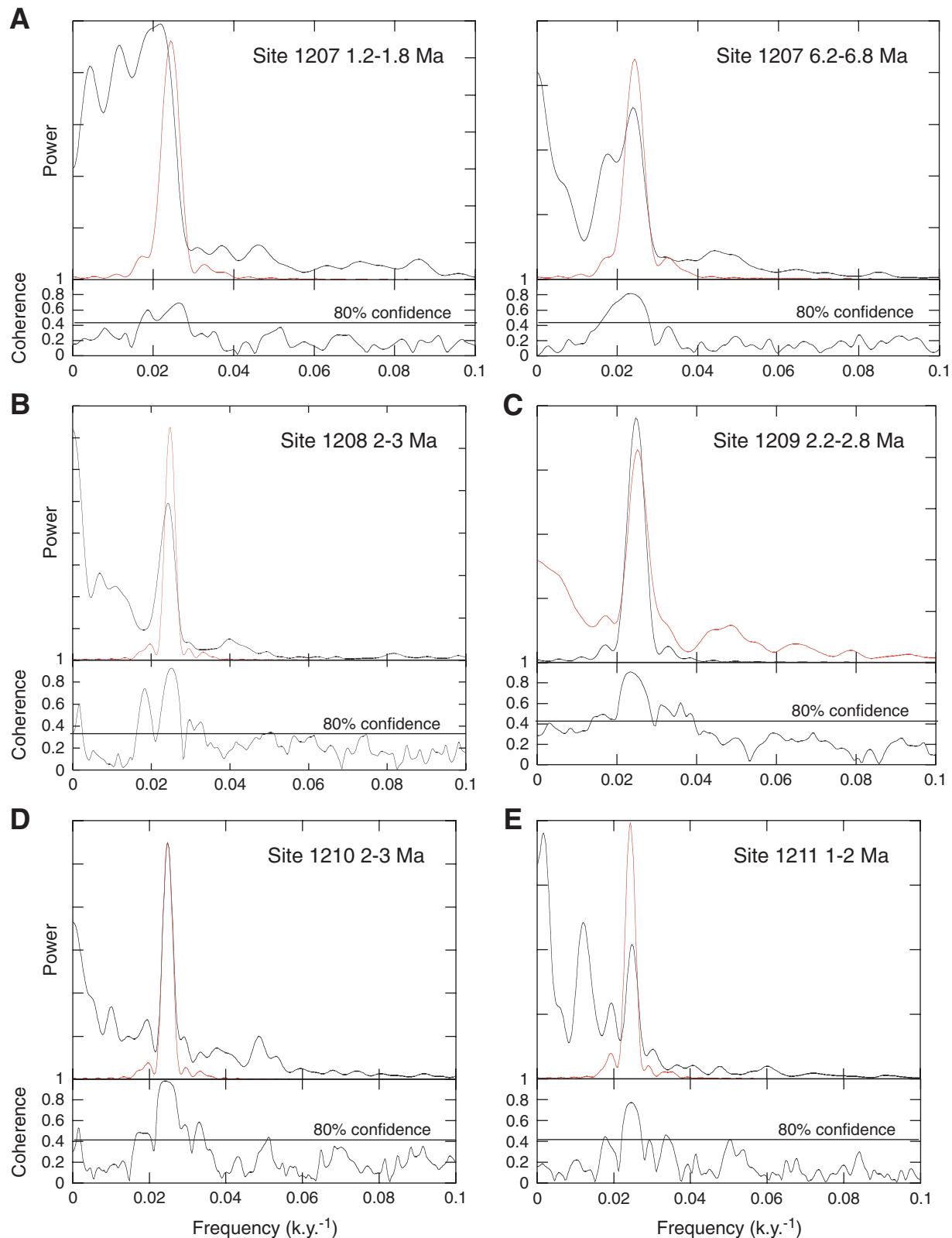


Table T1. Site location, oldest Neogene magnetic polarity chron identified, and basal age of Neogene section.

Site	Latitude	Longitude	Water depth (m)	Basal chron	Basal age (Ma)
1207	37°47.4287'N	162°45.0530'E	3100	C5An2n	12.184
1209	32°39.1001'N	158°30.3560'E	2387	C3Bn	7.091
1210	32°13.4123'N	158°15.5618'E	2573	C3Bn	7.091
1211	32°0.1300'N	157°50.9999'E	2907	C3Bn	7.091
1212	32° 26.9000'N	157°42.7016'E	2682	C4n.2n	8.072

Table T2. Magnetostratigraphic age model for Sites 1207, 1209, 1210, 1211, and 1212.

Chron	Age (Ma)	Depth				
		Site 1207 (mbsf)	Site 1209 (mcd)	Site 1210 (mcd)	Site 1211 (mcd)	Site 1212 (mcd)
C1n	0	0	0	0	0	0
Base	0.78	12.35	11.28	14.89	8	11.95
C1r.1n	0.99	16.26	13.32	18.07	9.55	14.12
Base	1.07	16.77	14.22	19.71	10.27	14.98
C2n	1.77	24.38	25.28	32.03	16.74	23.62
Base	1.95	28.4	28.21	34.7	18.38	25.78
C2r.1n	2.197	29.73		37.68	23.7	26.95
Base	2.229	30.25		38.09	30.08	27.78
C2An.1n	2.581	43.13	37.69	46.51	30.9	32.61
Base	3.04	51.77	49.43	56.88	32.34	39
C2An.2n	3.11	53.25		58.52	33.98	39.81
Base	3.22	56.79		60.37	37.37	41.67
C2An.3n	3.33	58.77	52.34	61.81	41.17	43
Base	3.58	66.91	58.03	67.35	42.51	48.68
C3n.1n	4.18	80.23	66.22	75.36	43.94	
Base	4.29	83.34	68.23	77.62	44.66	
C3n.2n	4.48	87.19		80.9	46.92	
Base	4.62	90.46		82.34	49.28	
C3n.3n	4.8	92.39	73.24	83.78	50.72	
Base	4.89	94.32	74.08	85.42	51.7	
C3n.4n	4.98	96.84	75.59	86.45	52.69	
Base	5.23	99.95	78.76	91.17	53.8	
C3An.1n	5.894	105.73	82.94	94.05	54.29	54.44
Base	6.137	106.77	84.95	95.69	55.15	56.17
C3An.2n	6.269	109.29	86.12	97.02		58.31
Base	6.567	114.18	90.13	99.12		59.14
C3Bn	6.935	116.56	93.81	100.35		59.88
Base	7.091	120.41	96.15	101.46		61.03
C3Br.1n	7.135				61.6	
Base	7.17				63.58	
C3Br.2n	7.341	123.08			64.57	
Base	7.375	123.53			65.14	
C4n.1n	7.432	125.16			65.39	
Base	7.562	126.05			66.95	
C4n.2n	7.65	126.34			67.37	
Base	8.072	129.01		70		
C4r.1n	8.225	130.79				
Base	8.257	132.27				
C4An	8.699	134.5				
Base	9.025	136.72				
C4Ar.1n	9.23	137.76				
Base	9.308	138.35				
C4Ar.2n	9.58	140.28				
Base	9.642	140.72				
C5n.1n	9.74	141.32				
Base	9.88	142.36				
C5n.2n	9.92	142.65				
Base	10.949	151.4				
C5r.1n	11.052	153.62				
Base	11.099	154.07				
C5r.2n	11.476	155.11				
Base	11.531	155.4				
C5An.1n	11.935	157.81				
Base	12.078	160.77				
C5An.2n	12.184	161.76				
Base	12.401					

Notes: Polarity chron labels are according to Cande and Kent (1992, 1995). Ages of chronos are from Cande and Kent (1995).

Table T3. Comparison of astrochronological age models for Sites 1207–1211.

Chron	Age (ka)					
	CK95 (Hilgen 1991a, 1991b)	Site 1207	Site 1208	Site 1209	Site 1210	Site 1211
C1n	0	0				
C1r.1r	780	776.7 (-3.3)				
C1r.1n	990	992.8 (2.8)				
C1r.2r	1070	1089.4 (19.4)	1073.9 (3.9)	1069.4 (-0.6)		
C2n	1770	1786.4 (16.4)	1776.2 (6.2)	1770.0 (0)	1777.8 (7.8)	1777.8 (7.8)
C2r.1r	1950	1954.2 (4.2)	1948.7 (-1.3)	1975.4 (25.4)	1972.2 (22.2)	1972.2 (22.2)
C2r.1n	2140	2095.7 (-44.3)	2133.5 (-6.5)			
C2r.2r	2150	2112.0 (-38)	2170.4 (20.4)			
C2An.1n	2581	2620.5 (39.5)	2564.7 (-16.3)	2550.3 (-30.7)	2642.7 (61.7)	2536.1 (-44.9)
C2An.1r	3040	3042.5 (2.5)	3045.2 (5.2)	3032.0 (-8)	3032.9 (-7.1)	3022.2 (-17.8)
C2An.2n	3110	3118.0 (8)	3105.8 (-4.2)		3114.9 (4.9)	3110.9 (0.9)
C2An.2r	3220	3236.5 (16.5)	3229.8 (9.8)		3248.5 (28.5)	3242.3 (22.3)
C2An.3n	3330	3354.5 (24.5)	3340.9 (10.9)	3361.4 (31.4)	3340.5 (10.5)	3352.8 (22.8)
C2Ar	3580	3593.3 (13.3)	3599.6 (19.6)	3648.8 (68.8)	3597.5 (17.5)	3644.4 (64.4)
C3n.1n	4180	4154.0 (-26)	4190.9 (10.9)	4172.5 (-7.5)	4182.8 (2.8)	4169.4 (-10.6)
C3n.1r	4290	4262.5 (-27.5)	4351.9 (61.9)	4305.9 (43.4)	4305.9 (15.9)	4305.6 (15.6)
C3n.2n	4480	4489.8 (9.8)	4523.6 (43.6)		4501.0 (21)	4457.9 (-22.1)
C3n.2r	4620	4637.0 (17)	4683.8 (63.8)		4665.3 (45.3)	4589.3 (-30.7)
C3n.3n	4800	4760.5 (-39.5)	4806.9 (6.9)	4809.0 (9)	4798.8 (-1.2)	
C3n.3r	4890	4857.3 (-32.7)	4880.9 (-9.1)	4880.9 (-9.1)	4891.2 (1.2)	
C3n.4n	4980	4972.5 (-7.5)	4991.8 (11.8)	4981.5 (1.5)	4973.3 (-6.7)	4950.7 (-29.3)
C3r	5230	5245.4 (15.4)	5201.2 (-28.8)	5240.2 (10.2)		
C3An.1n	5894	5886.0 (8)	5952.7 (58.7)	5915.8 (21.8)		
C3An.1r	6137	6143.0 (6)		6073.9 (36.9)		
C3An.2n	6269	6241.5 (-27.5)		6318.3 (49.3)		
C3Ar	6567	6526.2 (-40.8)		6548.3 (-18.7)		
C3Bn	6935	6878.0 (-57)		6971.3 (35.3)		
C3Br.1r	7091	7095.8 (4.8)		7027.7 (-63.3)		
C3Br.1n	7135					
C3Br.2r	7170					
C3Br.2n	7341	7348.2 (8.2)				
C3Br.3r	7375	7388.3 (13.3)				
C4n.1n	7432	7453.5 (3.5)				
C4n.1r	7562	7540.9 (-21.1)				
C4n.2n	7650	7634.1 (15.9)				
C4r.1r	8072	8038.0 (-34)				

Notes: Bold = most reliable ages in intervals where cyclicity in reflectance is best defined. Italics = differences between tuned ages and those of Cande and Kent (1995).

Table T4. Astrochronological ages for Leg 198 compared to published ages.

Chron	Age (ka)			
	(CK95) Hilgen (1991a, 1991b)	Leg 198	Shackleton et al. (1995)	Hilgen et al. (1995)
C1n	0			
Base	780	776.7		
C1r.1n	990	992.8		
Base	1070	1089.4		
C2n	1770	1786.4		
Base	1950	1954.2		
C2r.1n	2140	2133.5		
Base	2150	2170.4		
C2An.1n	2581	2564.7		
Base	3040	3042.5	3046 (3.5)	
C2An.2n	3110	3118	3131 (13)	
Base	3220	3236.5	3233 (-3.5)	
C2An.3n	3330	3354.5	3331 (-23.5)	
Base	3580	3593.3	3594 (0.7)	
C3n.1n	4180	4190.9	4199 (8.1)	
Base	4290	4351.9	4316 (-35.9)	
C3n.2n	4480	4523.6	4479 (-44.6)	
Base	4620	4683.8	4623 (-60.8)	
C3n.3n	4800	4806.9	4781 (-25.9)	
Base	4890	4880.9	4878 (-2.9)	
C3n.4n	4980	4972.5	4977 (4.5)	
Base	5230	5201.2	5232 (30.8)	
C3An.1n	5894	5952.7	5875 (-77.7)	
Base	6137	6143	6122 (-21)	
C3An.2n	6269	6241.5	6256 (14.5)	
Base	6567	6526.2	6555 (28.8)	6677 (150.8)
C3Bn	6935	6878	6919 (41)	7101 (223)
Base	7091	7095.8	7072 (-23.8)	7210 (114.2)
C3Br.1n	7135			7256
Base	7170			7301
C3Br.2n	7341	7348.2	7455 (106.8)	
Base	7375	7388.3		7492 (103.7)
C4n.1n	7432	7453.5	7406 (-47.5)	7532 (78.5)
Base	7562	7540.9	7533 (-7.9)	7644 (103.1)
C4n.2n	7650	7634.1	7618 (-16.1)	7697 (62.9)
Base	8072	8038	8027 (-11)	8109 (71)

Notes: Italics = differences between Leg 198 tuned ages and Hilgen et al. (1995) and Shackleton et al. (1995).

Table AT1. Paleomagnetic data, Site 1207. (Continued on next two pages.)

Depth (mbsf)	Steps (N)	Maximum angular deviation	Tensor-corrected component declination (°)	Component inclination (°)	Depth (mbsf)	Steps (N)	Maximum angular deviation	Tensor-corrected component declination (°)	Component inclination (°)
1.17	9	1.3	8.6	51.3	35.57	5	8.4	317.78	-72
1.88	9	1.7	27.3	66.1	36.04	7	9	152.68	-58.3
2.41	10	2.9	26.6	51.9	36.55	6	6.3	169.08	-56.3
2.78	10	3.8	21.2	63.2	37.04	3	18.1	233.58	-36.7
3.21	10	3.2	12.2	51	37.52	5	9.4	201.38	-50.5
3.75	11	7.8	352.1	58.5	38.05	5	8.6	167.28	-32.5
4.3	10	4.4	11.7	50.4	38.57	6	6.6	185.38	-55.1
5.26	10	1.4	356.8	66	39.03	9	4.8	160.88	-48.8
5.75	4	3.1	18.4	64.2	39.5	8	4.7	155.78	-55.1
6.15	9	2.8	15.9	53.7	40.04	4	5.4	167.18	-72.3
6.6	10	2.9	19.6	65.8	40.51	6	4.6	152.58	-61.8
7.07	11	1.6	28.8	73.4	41.04	9	8.1	46.48	-77.9
7.53	11	3.7	2	63.6	41.54	7	10.8	148.98	-55.3
8.1	11	2.9	10.5	61.4	42.06	4	8.4	295.98	37.4
8.6	12	1.1	22	60.9	42.54	8	6.2	134.68	-63
9.04	11	1.4	357.1	62.9	43.04	6	10	115.82	-15.6
9.6	11	2.9	7.6	54.9	43.53	6	8	293.82	56.6
10.05	10	2.2	22.9	57	44.04	8	8.4	288.72	60.4
10.55	10	2	28.1	59.3	44.54	6	6.5	300.02	47.7
11.05	7	6	8	51.7	45.04	8	5.2	311.92	58.4
11.55	10	3	26.4	68.9	45.54	6	10.6	322.52	68.4
12.05	10	2	32.4	59.3	46.02	4	9.2	347.12	68.7
12.55	9	4.4	227.8	-59.2	46.54	7	11.4	304.92	71.5
13.05	4	7.4	231.9	-42.4	47.04	10	4	302.22	52.1
13.55	9	2.1	215.9	-52.6	47.54	10	6	310.12	51.2
14.05	7	5.7	324	-75.3	48.05	9	23.6	270.62	43.5
14.85	5	9.9	283.4	-30.1	48.54	6	11.7	318.62	47.3
15.05	9	1.6	342.7	-47	49.01	7	7	339.42	58.8
15.55	10	3.2	325.1	-50.4	49.55	10	8.8	336.42	45.9
16.05	10	2.5	335.5	-48.7	50.04	10	4.3	319.22	56.5
16.55	6	18.2	336.9	77.5	50.54	10	6.6	335.42	50.4
16.99	9	4.3	332.8	-57.8	51.04	10	7.6	308.12	62.7
17.55	7	5.1	319.9	-25.2	51.5	10	7.9	338.42	49.9
18.08	9	1.8	333.1	-49.7	52.04	2	1.4	225.22	-8.1
18.56	7	4.5	328.1	-49.7	52.55	5	17.1	173.36	62.2
19.05	8	4	321.7	-47.2	53.05	3	3.3	150.36	-24.1
19.55	10	1.8	329.8	-52.7	53.55	2	10.6	174.46	45
20.06	9	2.5	331	-39.6	54.05	10	7.3	306.86	58.4
20.54	7	3.2	326.2	-44.1	54.55	9	8	307.66	46.6
21.07	9	2.5	321.5	-50.8	55.05	8	7.2	304.56	51.4
21.56	8	5.5	324.8	-26.6	55.55	11	8.1	322.36	64.1
22.05	7	4.2	325.3	-46.7	56.05	5	4.3	291.06	48.1
22.55	7	5.9	324.8	-41.9	56.55	2	20.2	106.06	59.9
23.05	4	6	0.1	-43	57.05	3	8.2	177.36	-52.4
23.55	10	3	318.5	-44.8	57.55	2	14.6	146.26	-32.7
24.06	8	2.9	133.74	-80.8	58.05	5	7.9	165.76	-36.1
24.56	10	1.6	321.64	58.5	58.55	1	0	152.96	-60
25.01	10	3.6	318.84	62	59.05	8	6.7	294.36	55.7
25.54	10	2.2	333.24	51.6	59.55	8	5	316.56	56.1
26.11	9	1.7	327.04	56.8	60.05	10	4.4	296.06	52.6
26.45	10	2.7	317.14	60	60.55	10	8.4	293.86	73.5
27.04	10	3	323.94	61.4	61.05	10	4.8	310.26	54.6
27.43	10	1.6	334.14	56.6	61.55	10	3.1	307.26	64.2
28.03	10	6.3	350.14	67.6	62.55	8	4.2	348.83	64.4
28.71	4	20.3	154.14	-59.3	63.05	10	4	3.33	60.7
29.04	8	4.1	155.04	-55.9	63.55	10	6	330.43	66.3
29.47	10	3.1	149.44	-46.4	64.05	10	4.6	345.73	68.8
30.04	6	6	337.14	37.3	64.55	11	5	6.63	74.5
30.43	1	0	3.84	-53.5	65.05	8	5.7	324.43	61.2
31.04	7	5.3	295.34	-74.6	65.55	10	3.3	348.23	59.1
32.07	5	6.5	190.64	-66.6	66.05	10	4.6	1.83	63.3
32.54	5	14.7	219.94	-83.4	66.55	9	4.2	258.43	77
33.03	5	13.3	253.44	-65.2	67.05	7	4.7	164.43	-44.5
33.55	6	13.6	282.44	62.1	67.55	9	1.9	163.13	-51.8
33.55	7	8.2	106.08	-60.8	68.05	9	2.6	167.93	-58.2
34.07	7	6.6	154.88	-79.9	68.55	6	6.5	147.03	-48.8
34.54	5	9.4	83.48	-77.2	69.05	10	2.5	166.83	-53.6
35.05	6	8.8	161.08	-67.1	69.55	6	5.8	148.03	-55.7

Table AT1 (continued).

Depth (mbsf)	Steps (N)	Maximum angular deviation	Tensor-corrected component declination (°)	Component inclination (°)	Depth (mbsf)	Steps (N)	Maximum angular deviation	Tensor-corrected component declination (°)	Component inclination (°)
70.05	8	4	181.93	-56.5	103.55	6	2.7	153.48	-48.2
70.55	9	3.1	163.93	-41.4	104.05	6	7.1	156.58	-49
71.55	10	2.4	178.49	-55.9	104.55	6	4	154.98	-48.8
72.05	10	5.1	162.49	-53.8	105.05	5	3.5	160.58	-46.3
72.55	6	6.3	173.39	-30	105.55	6	2	168.98	-58
73.05	5	4.6	154.69	-54.3	106.05	4	6.1	190.68	-60.2
73.55	5	5.1	164.49	-55.9	106.55	4	3.1	176.58	-44.8
74.05	5	6.4	165.29	-39.7	107.05	2	6.4	234.88	-50.3
74.55	3	8.6	169.59	-51.7	107.55	6	3	165.18	-43
75.05	5	9.1	164.69	-47.7	108.05	4	6.5	160.98	-54.5
75.55	5	5.3	152.59	-41.6	108.55	4	7.7	169.78	-44.4
76.05	9	4.5	156.29	-51.8	109.05	6	2.5	143.28	-48.1
76.55	9	3.8	156.99	-57.7	109.53	4	5.9	52.88	58.9
77.05	7	7.3	148.29	-48.8	110.05	12	4	332.53	59.3
77.55	4	5.4	148.39	-42	111.55	9	10.9	343.93	44.3
78.05	5	10.2	148.39	-47.8	113.05	12	3.9	321.23	57.7
78.55	4	10.5	138.79	-56.1	114.55	10	5.3	156.13	-47.2
79.05	2	2.4	139.59	-45.7	116.05	10	4.3	141.13	-48.8
79.55	2	6.9	139.09	-36.5	119.55	3	12.2	307.77	-8.3
80.05	3	3.4	151.09	-43.1	121.05	10	3.1	159.97	-52.6
80.55	2	2.9	86.79	72.4	122.55	10	1.5	169.87	-58.5
81.05	4	5.1	310.93	47.7	124.05	9	3.9	167.57	-49.1
81.55	5	7.3	306.73	57.1	127.05	11	6.6	328.77	49.6
82.05	4	19.1	270.23	47.5	129.05	7	7.8	165.73	-50
82.54	6	9.2	246.73	-20.6	129.55	11	4.7	166.93	-34.3
83.05	4	13.6	326.93	69.5	130.55	4	10.6	92.23	-76.4
83.55	5	9.5	206.73	-49.1	131.05	9	3.9	10.53	59.4
84.05	3	3.8	81.33	-71	132.05	14	5.4	347.63	65.7
84.55	5	10.6	170.13	-59.7	132.55	10	6.8	165.03	-41.7
85.05	1	0	157.83	-40.5	133.55	10	5.8	164.73	-46
85.55	5	9.3	145.33	-42.9	134.05	7	4.3	184.83	-45.9
86.05	3	6.1	148.63	-42	135.05	5	6.9	328.63	71.2
86.55	5	7.8	162.63	-64.6	135.55	18	1.7	2.43	59.8
87.05	3	3.6	168.83	-49.9	136.55	9	1.7	5.73	63
87.55	5	5.4	342.03	67.1	137	4	5.4	159.03	-25.3
88.05	2	3.2	357.43	59.8	137.55	1	0	102.93	-52.7
88.55	7	4.5	331.03	63.8	138.04	10	1.7	350.72	62.9
89.05	6	2.9	336.93	57.2	138.54	9	2.6	203.62	-45.7
89.55	6	2.1	329.63	60.1	139.04	3	13.9	191.22	-45.2
89.55	4	9.7	150.43	-47.7	139.54	9	1	172.72	-58.7
90.05	6	7.5	15.63	83.9	140.04	4	2.6	180.62	-42.9
90.55	6	5.5	154.18	-22.2	140.54	4	2.3	324.92	43.4
91.05	3	2.6	166.08	-60.7	141.04	9	4.8	210.92	-61.4
91.55	6	5.8	182.78	-54.3	141.54	11	2.6	327.02	49.2
92.04	5	3.7	170.78	-59.4	142.04	11	2.5	305.42	51.7
92.55	6	6.5	348.68	54.9	142.54	2	11.8	13.72	-11.3
93.05	7	4.1	357.48	59.9	143.04	11	2.5	330.22	57.9
93.55	6	1.8	335.38	60	143.54	13	5.9	310.12	50.5
94.05	6	1.6	337.18	55.6	144.04	13	1.9	312.32	53.1
94.54	4	4.4	142.58	-52	144.54	4	5.6	303.92	46.1
95.05	5	6.4	148.88	-58.4	145.04	3	8.6	310.72	34.5
95.54	6	4	156.38	-55.6	145.54	13	3.1	328.52	61.6
96.05	5	3.8	161.88	-48.2	146.04	13	3.3	324.12	63.6
96.54	2	7.1	357.88	-61.3	146.56	2	7.4	326.82	29.2
97.05	6	3.6	339.38	62.8	147.04	11	3.8	301.12	64.1
97.55	6	2.7	324.38	65.3	147.55	11	4.2	34.67	55.8
98.05	6	3	339.88	62.5	148.04	10	2.2	29.07	60.9
98.55	6	6.3	332.18	53.7	148.54	11	3.9	23.87	59.3
99.05	6	6.6	322.28	65.4	149.04	11	3.7	11.37	61.7
99.55	6	1.7	334.18	59.7	149.54	9	7.1	210.67	-60
99.99	6	6	346.48	69.7	150.04	11	7.1	6.77	63.5
100.05	5	3.8	174.68	-54.3	150.54	11	2.3	2.67	66.5
100.54	6	3	177.78	-43.5	151.04	10	3.7	9.77	58.2
101.05	6	3.7	175.68	-50.8	151.54	6	8.8	175.87	-48.9
101.54	5	2.9	169.48	-45.5	152.04	9	5.2	189.87	-57
102.05	5	10.1	180.98	-43.6	152.54	8	5.4	177.77	-58.3
102.55	6	4.6	181.78	-47.3	153.04	9	3.9	190.57	-60.9
103.05	6	2.7	167.68	-48.4	153.54	5	6.2	173.57	-78.7

Table AT1 (continued).

Depth (mbsf)	Steps (N)	Maximum angular deviation	Tensor-corrected component declination (°)	Component inclination (°)
154.04	7	9.7	187.27	-35.7
154.54	9	3.6	184.37	-58.9
155.04	6	6	197.47	-44.1
155.54	6	6.1	177.47	-60.6
156.04	3	24.7	109.77	-69.2
156.54	9	5.4	185.77	-53.7
157.55	4	11.1	196.61	-43.9
158.05	3	6.4	323.51	80.6
158.55	10	5.4	359.21	66.1
159.05	10	2.9	358.81	62.7
159.55	10	1.5	340.31	61.3
160.05	11	6.1	20.91	82.6

Table AT2. Paleomagnetic data, Site 1209. (Continued on next page.)

Depth		Maximum angular deviation	Tensor-corrected component declination (°)		Component inclination (°)	Depth		Maximum angular deviation	Tensor-corrected component declination (°)		Component inclination (°)
(mbsf)	(mcd)					(mbsf)	(mcd)				
0.39	0.39	3.5	358.7	69.1	54.74	59.45	3.9	184.79	-35.7		
1.1	1.1	4.1	337.8	44.8	56.1	62.11	2.7	182.5	-39.2		
1.89	1.89	4.4	347.1	45.1	56.8	62.81	2.6	184.4	-39.7		
2.6	2.6	2.4	339.8	67.9	57.6	63.61	2.8	182.7	-45		
3.39	3.39	3.1	345	40.9	58.3	64.31	1.7	183.6	-43.9		
4.1	4.1	1.8	332.6	53.4	59.1	65.11	2.1	183.4	-41.3		
4.89	4.89	1.6	334.5	47.6	59.8	65.81	3.1	181.5	-41.3		
5.6	5.6	3.8	341.3	48.7	60.6	66.61	4.7	343.2	61.1		
6.39	6.39	1.4	336.7	49.1	61.3	67.31	4.9	347.2	51.4		
6.9	6.9	1.7	326.5	50.2	62.1	68.11	17.7	271.9	21		
7.39	7.39	1.5	343.5	46.1	62.8	68.81	2.9	185	-44.5		
9.24	9.32	1.6	349.7	58.6	63.6	69.61	2.5	180.7	-42		
10.05	10.13	1.7	23.7	52.6	64.3	70.31	3.3	182.1	-47		
10.74	10.82	3.5	33.9	55.7	65.1	71.11	1.9	174.9	-42.2		
11.55	11.63	2.2	175.4	-55.4	65.59	72.18	9.8	186.65	-46		
12.27	12.35	4.3	161.5	-69.7	66.3	72.89	1.2	163.55	-49.6		
13.08	13.16	1.2	176.6	-48.1	67.09	73.68	1.9	342.05	50.8		
13.74	13.82	1.9	344.9	48.4	67.8	74.39	3.5	165.05	-47.2		
14.58	14.66	1.3	168.7	-53.1	68.59	75.18	3.5	158.85	-46.5		
15.24	15.32	2.4	167.9	-53.7	69.3	75.89	6.3	300.45	61.8		
16.08	16.16	4.6	141.8	-26.1	70.09	76.68	6.6	322.35	71.3		
16.74	16.82	1.5	164.1	-43	70.8	77.39	3.3	329.05	53.5		
18.05	21.11	1.5	33.9	-28.3	71.59	78.18	2.6	321.25	55.6		
18.59	21.65	6.5	14.4	-43.4	72.3	78.89	7.4	143.05	-32		
19.53	22.59	2.6	335.3	-43.9	73.09	79.68	7.7	177.05	-58		
20.25	23.31	1.9	328.3	-44.6	73.8	80.39	8	112.25	-60.8		
21.05	24.11	3.5	340.6	-52.9	74.5	81.09	2	154.45	-47.7		
21.74	24.8	1.4	330.5	-53.6	75.04	82.66	1.8	161.28	-46.1		
22.53	25.59	1.2	147.1	49.9	75.74	83.36	9.8	24.38	50.7		
23.27	26.33	1.4	148.4	41.4	76.55	84.17	2.5	349.38	57.2		
24.03	27.09	0.5	143.4	53.9	77.24	84.86	5.1	169.08	-35.4		
24.78	27.84	3.6	127.3	67.9	78.04	85.66	5	167.88	-26.5		
25.55	28.61	4.3	353.8	-54.3	78.7	86.32	5.6	165.18	-29.6		
26.28	29.34	3.1	6.1	-44.6	79.55	87.17	1.8	3.88	55.2		
27.74	31.41	3.1	142.61	-21.6	80.24	87.86	4.1	8.18	57.5		
28.14	31.81	2.2	185.01	-50.3	81.05	88.67	5.2	13.88	49.9		
28.9	32.57	5.3	184.41	-47.6	82.54	90.16	7.2	164.58	-36.7		
29.92	33.59	11	192.81	-41.2	83.24	90.86	5.8	165.58	-42.4		
30.54	34.21	4	184.31	-44.7	84.44	92.73	3.9	157.71	-46.5		
31.24	34.91	4.3	190.41	-35.7	85.24	93.53	8.1	242.51	-52.1		
32.29	35.96	6	187.71	-50.9	85.94	94.23	3.8	337.51	52		
32.87	36.54	7.1	176.11	-41	86.74	95.03	4.1	344.01	50.5		
33.53	37.2	5	151.41	-35.7	87.44	95.73	7.7	320.21	51.9		
34.54	38.21	4.7	318.91	56.9	88.24	96.53	3.5	146.61	-37.6		
35.04	38.71	4.8	331.01	58.7	88.94	97.23	4.5	163.71	-41.8		
35.74	39.41	3.6	349.01	56.5	89.74	98.03	15.3	288.11	65.7		
37.04	40.9	5.4	23.17	11	90.44	98.73	1.9	328.31	42.9		
37.75	41.61	3.8	342.07	51.7	91.24	99.53	7	171.71	-39.6		
38.54	42.4	4	349.57	67.5	91.94	100.23	3	324.81	54.5		
39.25	43.11	4.9	13.37	44.8	92.74	101.03	10.7	158.31	-57.8		
40.04	43.9	5.7	348.07	57.3	94.74	104.92	3.1	22.26	63		
40.75	44.61	5	358.07	55.5	95.44	105.62	3.8	17.06	59.7		
41.53	45.39	4.2	16.97	52.1	95.44	105.62	3.3	1.36	51.1		
42.24	46.1	3.5	0.57001	56.5	96.24	106.42	13.3	72.16	68.1		
43.04	46.9	6.9	351.87	51.7	96.94	107.12	7	163.16	-37.1		
43.74	47.6	10.1	30.27	60.6	97.74	107.92	7.8	42.96	63.3		
44.54	48.4	6.9	35.87	52.7	98.44	108.62	2.6	358.56	58.6		
45.24	49.1	3.8	12.67	51.9	99.24	109.42	7.1	144.76	-30.3		
47.24	51.95	2.9	180.29	-48.8	99.94	110.12	8.2	162.16	-25		
48.09	52.8	7.7	304.99	67.7	100.74	110.92	7.1	166.66	-31		
48.74	53.45	6.2	338.89	60.8	101.44	111.62	4.9	140.06	-6.3		
49.59	54.3	4.7	357.49	50.3	102.24	112.42	5.6	22.06	68.4		
50.24	54.95	6	345.19	53.8	103.44	112.8	25.7	332.94	34.4		
51.09	55.8	3.7	344.49	58.1	102.94	113.12	3.5	169.56	-34.9		
51.74	56.45	4	0.98999	58.7	104.24	113.6	9.1	147.04	-34.6		
52.59	57.3	5.2	348.29	66.9	104.94	114.3	2	339.94	50.7		
53.24	57.95	7.9	321.49	41.1	105.74	115.1	8.3	136.94	-38.6		
54.09	58.8	2.3	181.29	-51.1	106.44	115.8	4.6	78.24	35.1		

Table AT2 (continued).

Depth (mbsf)	Maximum angular deviation	Tensor-corrected component declination (°)	Component inclination (°)
107.24	116.6	3.6	340.04
107.94	117.3	6	345.84
108.74	118.1	15.9	160.84
109.44	118.8	19.4	77.84
109.74	119.1	5.8	8.74
110.24	119.6	3.8	333.14
110.94	120.3	14.5	20.24

Table AT3. Paleomagnetic data, Site 1210. (Continued on next page.)

Depth		Maximum angular deviation	Tensor-corrected component		Depth		Maximum angular deviation	Tensor-corrected component	
(mbsf)	(mcd)		declination (°)	inclination (°)	(mbsf)	(mcd)		declination (°)	inclination (°)
0.48	0.48	1.5	283.1	50.3	53.42	57.94	1.5	148.95	-41
1.03	1.03	1.2	276.9	65.3	53.82	59.37	3.3	331.54	55.6
1.98	1.98	3.1	286.5	52	54.58	60.13	4.2	334.64	54.3
2.53	2.53	2.1	252.3	60.5	55.32	60.87	2.6	157.94	-56.5
3.48	3.48	3.4	264.1	67.8	56.08	61.63	1.3	167.44	-37.7
4.03	4.03	3.3	277.9	51.4	56.82	62.37	2.6	12.14	74.4
4.98	4.98	1.8	267	52.9	57.58	63.13	2.8	337.94	46
6.38	7.89	3.7	78.6	56.8	58.32	63.87	1.1	353.54	65.8
6.94	8.45	2	70	50.7	59.08	64.63	3.1	338.04	52.4
7.88	9.39	1.1	83.9	52.5	59.82	65.37	1.4	333.74	60.4
8.44	9.95	1.2	94.4	55.2	60.58	66.13	3.4	324.84	64.6
9.38	10.89	1.5	85	59.5	61.32	66.87	1.7	328.74	60.7
9.94	11.45	1	86.7	56.8	62.08	67.63	4.6	143.64	-44
10.88	12.39	2.2	82.6	54.9	62.82	68.37	2.6	140.74	-38.1
11.44	12.95	1.6	107.6	56.6	63.3	69.59	4.8	171.44	-38.1
12.38	13.89	1.9	88.2	53.9	64.1	70.39	6.6	167.54	-36.8
12.94	14.45	1.3	92.9	52.9	64.8	71.09	2.4	156.74	-47.8
13.88	15.39	1.3	280.6	-52.2	65.6	71.89	5	171.14	-58.2
14.54	16.05	2.7	272.5	-53	66.3	72.59	1.9	154.04	-44
15.88	17.07	2.4	6.5	-44.2	67.1	73.39	3.8	140.04	-47.5
16.39	17.58	1.3	6.3	-48.1	67.8	74.09	1.6	156.64	-53.7
17.38	18.57	1.5	156.6	54.8	67.8	74.09	4.5	305.84	64.4
17.89	19.08	5.3	186.9	67.1	68.6	74.89	5.4	172.74	-21.6
18.88	20.07	1.4	348	-41.2	70.1	76.39	1	329.64	59
19.4	20.59	1.5	1.8	-53.5	70.8	77.09	2.1	327.64	63.1
20.45	21.64	0	30.7	-32.4	71.6	77.89	3.8	153.34	-29.1
20.89	22.08	3.8	31.6	-39.1	72.3	78.59	1.1	154.44	-47
21.89	23.08	1.8	22.2	-42.8	72.8	80.45	2.3	166.73	-43.1
22.39	23.58	1.1	19.4	-54.6	73.6	81.25	1.2	345.63	51.4
23.39	24.58	1.2	10.5	-46	74.3	81.95	1.4	345.73	54.2
23.89	25.08	2.1	17.2	-49.7	75.1	82.75	3.1	168.13	-45.3
25.3	27.58	2	153.21	-50.6	75.8	83.45	3	173.33	-40
26.06	28.34	1.9	170.31	-59.1	76.6	84.25	3.5	336.03	55.8
26.8	29.08	0.8	166.21	-55	77.3	84.95	1.3	350.33	50.5
27.56	29.84	1.3	163.61	-49.1	78.1	85.75	2.9	172.53	-43.3
29.06	31.34	0.9	161.11	-53.5	78.8	86.45	13.6	33.03	8.1
29.8	32.08	3.9	166.21	-52.1	79.6	87.25	4.5	305.93	65.3
29.8	32.08	1.1	321.11	49.5	80.3	87.95	1.5	335.43	58
30.56	32.84	1.7	333.01	47.6	81.1	88.75	6.2	353.03	70.9
31.3	33.58	2.1	333.11	55.2	82	90.26	0.9	319.65	59
32.06	34.34	3.1	323.01	57	82.29	90.55	3	322.75	60.6
32.7	34.98	1.7	149.61	-42.2	82.7	90.96	2.7	327.25	57.7
33.56	35.84	3	158.31	-56.3	82.94	91.2	5	133.35	-40.4
34.3	36.58	2.5	158.81	-47.6	83.23	91.49	1.9	151.65	-41.8
35.58	38.68	2.3	163.56	-49.7	83.5	91.76	5.5	152.35	-49.7
36.3	39.4	2.1	157.96	-52.1	83.76	92.02	1.6	145.05	-46.8
37.08	40.18	2.4	162.36	-45.7	84.2	92.46	2.4	137.45	-52.9
37.8	40.9	3	158.56	-50	84.44	92.7	3.2	145.55	-44.2
38.64	41.74	1.6	148.76	-47.4	84.73	92.99	1.9	149.05	-44.7
39.3	42.4	6.3	222.06	-70.2	85	93.26	13.7	114.75	-6.5
40.17	43.27	2	159.76	-49.9	85.29	93.55	17.7	148.95	-28.2
40.8	43.9	2.5	151.86	-45.5	85.7	93.96	3	133.85	-47
41.57	44.67	3.5	149.56	-39	85.92	94.18	2.5	336.75	56.8
42.3	45.4	7.9	171.86	-55.7	86.23	94.49	1.8	330.95	53.9
43.12	46.22	4.6	168.26	-47.3	86.5	94.76	4	319.55	45.1
43.8	46.9	2.8	332.86	65.4	86.79	95.05	2.4	333.95	61.8
44.42	48.94	2.1	329.55	53	87.2	95.46	1.3	331.15	50.1
45.08	49.6	1.1	338.25	57.9	87.44	95.7	2.2	330.15	42.7
45.92	50.44	1.6	339.15	53.3	87.44	95.7	1.5	153.15	-45.6
46.58	51.1	1.2	331.45	55.9	87.73	95.99	3.7	147.05	-47
47.42	51.94	1	335.05	55.3	88	96.26	2.3	154.35	-50.2
48.08	52.6	1.8	334.45	52.8	88.29	96.55	2	140.65	-46
48.92	53.44	2.8	327.05	55.8	88.7	96.96	1.9	154.15	-39.1
49.58	54.1	1.3	329.45	51.8	89.23	97.49	0.9	326.15	54.3
50.42	54.94	1.2	330.15	54.6	89.5	97.76	2.5	327.45	51
51.08	55.6	0.8	326.55	50	89.79	98.05	1.7	326.05	53.5
51.92	56.44	1.1	323.35	50.9	90.2	98.46	3.2	325.85	52.7
52.58	57.1	2	148.75	-32.1	90.44	98.7	7.1	329.95	48.6

Table AT3 (continued).

Depth (mbsf)	Maximum angular deviation	Tensor-corrected component declination (°)	Component inclination (°)
90.73	98.99	3	338.65
91	99.26	3.1	149.65
91.43	99.69	1.7	153.85
91.79	101.35	6.6	333.73
92.03	101.59	12.6	162.53
92.44	102	3.9	147.83
92.72	102.28	3.9	327.53
93.09	102.65	5.2	152.63
93.29	102.85	5	150.53
93.38	102.94	8.1	141.03
93.88	103.44	2.3	334.73
94.19	103.75	3	338.43
94.79	104.35	13.2	305.13
95.18	104.74	3.6	164.83
95.38	104.94	5	167.53
95.74	105.3	3.2	162.43
96.29	105.85	20.5	283.33
96.54	106.1	2.9	339.33
96.88	106.44	2.2	338.43
97.2	106.76	3.7	348.83
97.79	107.35	7.7	159.73
98.14	107.7	7.7	168.73
98.72	108.28	3.4	353.93
99.05	108.61	4.4	332.43
99.29	108.85	5.9	171.63
99.55	109.11	3.1	18.83
99.84	109.4	5.1	159.73
100.55	110.11	2.9	358.63
101.05	110.61	8	119.68

Table AT4. Paleomagnetic data, Site 1211.

Depth		Maximum angular deviation	Tensor-corrected component declination (°)		Component inclination (°)	Depth		Maximum angular deviation	Tensor-corrected component declination (°)		Component inclination (°)
(mbsf)	(mcd)					(mbsf)	(mcd)				
0.2	0.2	1.1	345.3	46.6		34.74	38.84	3.6	165.21	-37.7	
0.75	0.75	3.2	320.3	40.7		35.5	39.6	1.1	152.31	-46.8	
1.18	1.18	1.3	324	39.1		36.24	40.34	3.4	159.01	-39.9	
1.7	1.7	4.2	350.3	30.1		37	41.1	2.3	167.11	-44.2	
2.25	2.25	2.6	84	35.7		37.74	41.84	2.3	338.71	55.5	
3.95	6.15	2	25.7	56.4		38.5	42.6	3.4	154.11	-51.5	
4.69	6.89	3.2	63.5	76.5		39.24	43.34	5.8	172.91	-40.2	
5.45	7.65	1.5	33	48		40	44.1	1.9	343.81	51.3	
6.19	8.39	1.9	224.9	-58.7		40.74	44.84	3	170.61	-45	
6.95	9.15	4.9	230	-67.2		41.15	46.55	2	143.34	-58.8	
7.69	9.89	2	54.8	53.5		41.58	46.98	1.7	339.14	50.8	
8.45	10.65	1.9	252.6	-55.4		42	47.4	2.8	321.84	50	
9.19	11.39	14.5	355.1	-20.3		42.65	48.05	3.6	338.34	51.2	
9.95	12.15	1.2	249.8	-50.8		43.08	48.48	5.7	345.14	57.4	
10.69	12.89	3.6	258.2	-43		43.5	48.9	1.1	344.04	40.4	
11.45	13.65	2	267.6	-51.5		44.15	49.55	2.9	155.14	-50.2	
12.65	15.35	2.7	318.4	-40.7		44.58	49.98	4.4	174.14	-48.8	
13.35	16.05	2.6	328	-42.2		45	50.4	6.4	163.44	-48.8	
14.15	16.85	1.4	150.9	51.8		45.65	51.05	2.3	352.44	46.9	
14.85	17.55	1.5	151.4	47.3		46.08	51.48	1.1	353.74	48.2	
15.65	18.35	1.9	342.9	-43.1		46.5	51.9	2.6	181.24	-54.8	
16.35	19.05	3.3	319.1	-46		47.15	52.55	6.1	175.84	-51.3	
17.15	19.85	1.4	328	-35.7		47.58	52.98	2.3	359.84	45.4	
17.85	20.55	2.3	327.9	-42.3		48	53.4	3.2	351.44	35.6	
18.65	21.35	1.5	342.8	-46.4		48.65	54.05	10.9	181.14	-44.7	
19.35	22.05	2.4	333.2	-43.3		49.08	54.48	4.9	1.54	44.9	
20.15	22.85	1.6	338.5	-45.2		49.5	54.9	2.8	7.64	37.7	
20.85	23.55	1.8	345.7	-38.9		50.15	55.55	1.9	11.74	43.3	
21.65	24.35	1.6	163.4	47.6		53.04	59.34	5.4	163	22	
22.23	25.63	3.3	3.67	54.1		53.39	59.69	3.2	213.6	10.4	
22.95	26.35	2.6	4.17	54.3		53.89	60.19	3.6	196.8	18.3	
23.73	27.13	2.2	19.17	51.1		54.39	60.69	2.4	198.3	6.9	
24.45	27.85	3.1	15.67	52.8		54.89	61.19	1.8	228.6	-17.6	
25.23	28.63	3.8	18.77	57.2		55.39	61.69	2	207.9	-7.1	
25.95	29.35	4.9	11.97	58.1		55.89	62.19	2.9	211.5	-12.9	
26.73	30.13	5	188.47	-50.8		56.39	62.69	2.1	203.1	10	
27.45	30.85	3.7	190.17	-32.8		56.89	63.19	4.2	192.8	6.1	
28.23	31.63	6.2	46.07	57		57.39	63.69	2.3	198.5	11.7	
28.95	32.35	9.7	31.07	68.6		57.89	64.19	3.6	196.5	21.9	
29.73	33.13	2	212.07	-46.7		58.39	64.69	1.5	206.7	-2.6	
30.45	33.85	2.7	206.37	-47.2		58.89	65.19	2.4	217.2	-4.7	
31.23	34.63	1.3	37.77	60.6		59.39	65.69	1.3	201	7.6	
31.74	35.84	1.7	334.91	53.6		59.79	66.09	3.2	195.4	23.6	
32.5	36.6	2.9	332.81	53.2		60.04	66.44	4.4	24.98	20	
33.24	37.34	1.8	341.21	52.6							
34	38.1	1.7	158.71	-47							

Table AT5. Paleomagnetic data, Site 1212.

Depth		Maximum angular deviation	Tensor-corrected component declination (°)		Component inclination (°)	Depth		Maximum angular deviation	Tensor-corrected component declination (°)		Component inclination (°)
(mbsf)	(mcd)					(mbsf)	(mcd)				
0.29	0.44	0.7	7.7	51.4		40.56	44.35	1.7	26.9	56	
1.25	1.4	2.1	-0.099998	42.4		41.4	45.19	5.3	48.3	70.5	
1.79	1.94	5.5	12.4	51.5		42.06	45.85	1.8	44.6	60.8	
2.75	2.9	1.3	0.099998	53.8		42.9	46.69	7.1	44.6	64.8	
3.29	3.44	2.2	10.8	51.2		45.24	49.03	3.6	162.58	-36	
3.87	4.02	2.8	3.8	51.7		45.7	49.49	6.8	172.08	-31.5	
4.29	4.44	1	7.3	56.3		46.27	50.06	5.8	171.78	-43.3	
5.38	8.53	1.6	363.4	54.4		46.79	50.58	6.1	189.78	-52.5	
6.07	9.22	1.2	362.9	52		47.2	50.99	4.4	163.88	-30.2	
6.88	10.03	2.5	356.4	51.6		47.51	51.3	2.6	176.18	-44.4	
7.57	10.72	1.6	358.8	50.6		47.77	51.56	2.6	176.68	-42.8	
8.38	11.53	1.1	365.8	42.5		48.34	52.13	4.1	182.38	-44.6	
9.07	12.22	4.7	157.9	-19.9		48.46	52.25	2.3	179.78	-45.5	
9.88	13.03	4.4	187.3	-35.1		48.77	52.56	4.7	172.58	-29.6	
10.57	13.72	1.5	188.2	-47.6		47.88	55.15	1.9	353.47	54.2	
11.38	14.53	2.4	397.5	48.4		48.38	55.65	5.9	347.77	60.4	
12.07	15.22	2.9	190.7	-38.9		49.38	56.65	3.3	172.17	-37.3	
12.88	16.03	4.2	153.2	-37		49.88	57.15	3.1	175.37	-44.1	
13.57	16.72	4.2	203.8	-41.2		50.24	57.51	5	184.67	-38.5	
14.38	17.53	2.5	201.4	-41.2		50.88	58.15	7.7	132.77	-40.2	
14.88	18.37	1.5	146.3	-54.8		51.25	58.52	2.3	332.67	59.3	
15.58	19.07	2.6	140	-44.9		51.38	58.65	6	345.17	56.5	
16.38	19.87	1.8	164.6	-53.9		51.74	59.01	1.9	343.67	41.9	
17.08	20.57	3.7	181.4	-57.2		52.1	59.37	1	172.37	-49.6	
17.88	21.37	1.6	159.1	-55.5		52.38	59.65	3.6	166.27	-47.5	
18.58	22.07	1.5	166.1	-47.5		52.75	60.02	3.3	341.17	49.5	
19.38	22.87	2.8	184.2	-50.6		52.88	60.15	12.3	338.47	60.2	
20.08	23.57	2.4	175.1	-56.9		53.24	60.51	5.9	7.57	64.5	
20.88	24.37	1.8	353.5	55.2		53.6	60.87	19.8	96.87	69.6	
21.58	25.07	1	4.3	57		53.88	61.15	2	175.17	-43.9	
22.38	25.87	1.8	194.7	-51.5		54.25	61.52	3.7	159.97	-44.9	
23.08	26.57	2.8	199.3	-59.5		54.38	61.65	1.6	1.57	49.9	
23.88	27.37	0.8	192.7	-50.5		54.74	62.01	2.6	359.77	44.1	
24.36	27.85	1.8	164.09	-41.7		55.1	62.37	1.7	355.17	49.8	
24.98	28.47	3.7	166.49	-48.6		55.38	62.65	2	357.57	46	
25.86	29.35	1.3	178.39	-58.1		55.75	63.02	1.8	3.27	44.5	
26.48	29.97	1.3	177.89	-47.7		55.88	63.15	1.4	358.47	55.6	
27.36	30.85	2.2	184.89	-47.7		56.24	63.51	2.8	182.87	-45.2	
27.98	31.47	1.5	190.99	-47		56.6	63.87	3.2	175.97	-41.9	
28.86	32.35	2.2	198.39	-41.5		57.13	64.98	2.3	352.01	54.2	
29.48	32.97	2.7	31.69	59		57.39	65.24	1.4	179.41	-46.9	
30.36	33.85	2.5	22.09	54.9		57.79	65.64	2.1	351.71	51.9	
30.98	34.47	2.6	35.39	62.2		57.89	65.74	5.6	357.81	60.6	
31.86	35.35	3.9	46.99	63		58.25	66.1	17.8	149.21	70.4	
32.48	35.97	3.8	43.79	57.5		58.63	66.48	6.2	339.21	63	
33.23	36.72	3	33.59	61.6		58.89	66.74	3.9	358.61	60.2	
33.9	37.69	1.3	9.3	57.2		59.29	67.14	4.2	171.21	-43.6	
34.56	38.35	1	7.2	55.2		59.39	67.24	4.2	183.01	-49.7	
35.4	39.19	3.2	186.9	-38.6		59.75	67.6	6.3	2.51	63.1	
36.06	39.85	6	194.4	-25.6		59.98	67.83	28.6	179.01	-14.4	
36.9	40.69	1.9	16.5	54.8		60.79	68.64	16.3	264.31	56.9	
37.56	41.35	4.3	22.7	65.1		61.74	69.59	3.5	284.81	66.3	
38.4	42.19	5.7	197	-34.8		62.15	70	1.8	350.11	55.5	
39.06	42.85	1.2	202.2	-46.6							
39.9	43.69	2.3	18.3	63.5							